



LAWRENCE
LIVERMORE
NATIONAL
LABORATORY

Spatially-Resolved Analyses of Aerodynamic Fallout from a Uranium-Fueled Nuclear Test

L. A. Lewis, K. B. Knight, J. E. Matzel, S. G. Prussin, M.
M. Zimmer, W. S. Kinman, F. J. Ryerson, I. D.
Hutcheon

April 29, 2015

Journal of Environmental Radioactivity

Disclaimer

This document was prepared as an account of work sponsored by an agency of the United States government. Neither the United States government nor Lawrence Livermore National Security, LLC, nor any of their employees makes any warranty, expressed or implied, or assumes any legal liability or responsibility for the accuracy, completeness, or usefulness of any information, apparatus, product, or process disclosed, or represents that its use would not infringe privately owned rights. Reference herein to any specific commercial product, process, or service by trade name, trademark, manufacturer, or otherwise does not necessarily constitute or imply its endorsement, recommendation, or favoring by the United States government or Lawrence Livermore National Security, LLC. The views and opinions of authors expressed herein do not necessarily state or reflect those of the United States government or Lawrence Livermore National Security, LLC, and shall not be used for advertising or product endorsement purposes.

Spatially-Resolved Analyses of Aerodynamic Fallout from a Uranium-Fueled Nuclear Test

L.A. Lewis^{a,b,1}, K.B. Knight^a, J.E. Matzel^a, S.G. Prussin^b, M.M. Zimmer^d, W.S. Kinman^c, F.J. Ryerson^a and I.D. Hutcheon^a

^a Glenn Seaborg Institute, Lawrence Livermore National Laboratory, 7000 East Avenue, Livermore, CA 94550, USA

^b Department of Nuclear Engineering, University of California, Berkeley, 4113 Etcheverry Hall MC 1730, Berkeley, CA 94720, USA

^c Los Alamos National Laboratory, P.O. Box 1663, Los Alamos, NM 87544, USA

^d Pacific Northwest National Laboratory, P.O. Box 999, Richland, WA 99352, USA

Highlights

- We measured the spatial distribution of U isotopes, major elements, and radioactivity in five glassy fallout spherules
- We used secondary ion mass spectrometry, electron microscopy, x-ray spectroscopy, and autoradiography
- In two spherules, the $^{235}\text{U}/^{238}\text{U}$ ratio is heterogeneous and correlated with major elements
- In two spherules, the $^{235}\text{U}/^{238}\text{U}$ ratio is approximately homogeneous
- These results reflect variable mixing within fallout spherules between U from the device and U from the soil
- We use these results to discuss the evidence and roles of various fallout formation processes

Keywords: SIMS; trinitite; fallout; device debris; nuclear forensics

Abstract

Five silicate fallout glass spherules produced in a uranium-fueled, near-surface nuclear test were characterized by secondary ion mass spectrometry, electron probe microanalysis, autoradiography, scanning electron microscopy, and energy-dispersive x-ray spectroscopy. Several samples display compositional heterogeneity suggestive of incomplete mixing between major elements and natural U ($^{238}\text{U}/^{235}\text{U} = 0.00725$) and enriched U. Samples exhibit extreme spatial heterogeneity in U isotopic composition with $0.02 < ^{235}\text{U}/^{238}\text{U} < 11.84$ among all five spherules, and $0.02 < ^{235}\text{U}/^{238}\text{U} < 7.84$ within a single spherule. In two spherules, the $^{235}\text{U}/^{238}\text{U}$ ratio is correlated with changes in major element composition, suggesting the agglomeration of chemically and isotopically distinct molten precursors. Two samples are nearly homogeneous with respect to composition and uranium isotopic composition, suggesting extensive mixing possibly due to experiencing higher temperatures or residing longer in the fireball. Linear correlations between $^{234}\text{U}/^{238}\text{U}$, $^{235}\text{U}/^{238}\text{U}$, and $^{236}\text{U}/^{238}\text{U}$ ratios are consistent with a two-component mixing model, which is used to illustrate the extent of mixing between natural and enriched U end members.

1. Introduction

There is renewed interest in post-detonation glassy fallout formed during surface and near-surface nuclear explosions (Parekh et al., 2006; Eby et al., 2010; Fahey et al., 2010; Belloni et al., 2011; Bellucci et al., 2012; Cassata et al., 2014; Eppich et al., 2014; Sharp et al., 2014). During the era of above ground nuclear testing, fallout analyses focused on understanding device performance and how radioactivity spread post-detonation. Techniques

¹Corresponding author. Tel.: +1 925-422-5377
E-mail address: lewis105@llnl.gov (Laurence Lewis).

44 for analyzing fallout on small spatial scales were generally limited to methods such as autoradiography to image the
45 distributions of fission and activation products (Adams et al., 1960). Today, using modern microanalytical
46 techniques, spatially-resolved analyses of post-detonation fallout from historic nuclear tests can provide much more
47 information on the distribution of stable and long-lived radioactive isotopes with the goal of a more comprehensive
48 understanding of fallout formation, such as improved constraints on formation mechanisms, timescales, and
49 temperatures (Cassata et al., 2014; Eppich et al., 2014).

50 Glassy fallout forms when a nuclear device is detonated on or near the Earth's surface. Surface detonations melt
51 large masses of environmental material (e.g., soil), which may remain in place or be swept into the nuclear fireball.
52 In both cases, the molten material may interact with device components, fission and activation products, and
53 unfissioned fuel (collectively 'device debris'; Brode, 1968; Glasstone and Dolan, 1977). As the fireball cools below
54 the melting point of the surrounding material, device debris becomes trapped within a fused glassy matrix and
55 rapidly cools, forming glassy fallout. Because the mass of melted environmental material can be much greater than
56 mass of the device in near surface events, the major element composition of these glasses can predominantly reflect
57 that of the local geology and/or emplacement environment, and device debris is generally present only in trace
58 quantities (Adams and O'Connor, 1957; Miller, 1964).

59 There are two main morphological classes of glassy fallout, referred to herein as ground glass and aerodynamic
60 glassy fallout. Ground glass usually exhibits a smooth, glassy surface with compositional variations often
61 transitioning to unmelted soil (Eby et al., 2010). This is consistent with either in-situ melting of soil and/or solid
62 material being swept into the fireball and incompletely melted, before raining back down onto the soil below
63 (Hermes and Strickfaden, 2005). In contrast, aerodynamic glassy fallout (also known as fallout beads or spherules)
64 usually appears glassy throughout and often exhibits spheroidal, near-spheroidal, or dumbbell shapes, consistent
65 with fusing and quenching while still aloft (Miller, 1960; Crocker et al., 1965; Tompkins et al., 1970; Fig. 1).
66 Aerodynamic glasses often have smaller glassy spheres attached to their surfaces, consistent with growth through
67 collisional processes and mixing of molten droplets within the fireball (Miller, 1964; Stewart, 1956). For
68 aerodynamic fallout, the cooling timescale depends on device yield, but is estimated (Glasstone et al., 1977; Izrael,
69 2002) and measured (Cassata et al., 2014) to be on the order of seconds. Few previous studies have focused
70 specifically on aerodynamic fallout glasses, but these objects are of particular interest due to their elevated
71 concentrations of residual fuel and fission and activation products (Mackin et al., 1958; Eppich et al., 2014). How
72 direct device components distribute themselves within aerodynamic fallout remains unaddressed.

73 Ground glass from the Trinity test, popularly referred to as 'trinitite', has been extensively studied over the past
74 decade (Parekh et al., 2006; Eby et al., 2010; Fahey et al., 2010; Belloni et al., 2011; Bellucci et al., 2012; Bellucci
75 et al., 2013; Wallace et al., 2013; Bellucci et al., 2014; Sharp et al., 2014). These studies demonstrate that trinitite is
76 a compositionally heterogeneous mixture of completely melted, partially melted, and unmelted minerals found in the
77 local geology, with the glassy and eddied portions of the trinitite containing most of the unfissioned Pu fuel and
78 fission products. Comparisons of trinitite with observations of aerodynamic fallout from Trinity (trinitite spherules),
79 or between aerodynamic and ground glass from other nuclear tests have yet to be reported.

80 In contrast to recent studies characterizing ground glass from the Pu-fueled Trinity test, this study characterizes
81 aerodynamic fallout glass from a U-fueled device. Bulk studies (analyses of dissolved spherules) of these materials
82 has been recently reported (Eppich et al., 2014). Here, we characterize the spatial distribution of unfissioned U fuel
83 within individual glassy fallout spherules using secondary ion mass spectrometry (SIMS) combined with scanning
84 electron microscopy/energy-dispersive x-ray spectroscopy (SEM/EDS), electron probe microanalysis (EPMA), and
85 autoradiography. For each spherule, we measured the extent of uranium isotopic heterogeneity, major element
86 composition, and radioactivity, and we correlate these observations with spatial locations within individual
87 spherules. The extent of mixing is quantified by assuming a model of two-component mixing between uranium from
88 the soil and/or device with enriched uranium from the device, and then calculating the relative contribution of each
89 end member to each U isotopic measurement. We use our collective results to discuss the evidence and role of
90 different mechanisms in fallout formation.

91

92 **2. Materials and methods**

93 **2.1 Fallout spherules**

94 Five millimeter-size fallout spherules were selected from soil collected at the site of a historic, uranium-fueled, near-
95 surface nuclear test. The soil samples were collected about 120 meters from ground zero along the path of the fallout

96 plume. Glassy fallout is easily identifiable in soil collections due to its smooth surface morphology and aerodynamic
97 shape (Fig. 1). The spherules were isolated from sieved soils by visual inspection and handpicked under an optical
98 microscope, then were weighed and photographed. Each spherule was mounted in epoxy and polished to expose an
99 interior surface close to the mid-plane of the object. Samples were coated with ~10-20 nm of carbon to prevent
100 charging, and then characterized by SEM/EDS, EPMA, autoradiography, and SIMS.

101
102 *[Figure 1 —Optical images of size-sorted fallout (left) showing distinct dark glassy aerodynamic*
103 *shapes mixed with soil fragments, and an isolated piece of aerodynamic fallout glass (right). The*
104 *bright artifact in the center of the isolated aerodynamic fallout glass is the ring light from the*
105 *optical microscope, which also highlights the high degree of symmetry in these objects.]*

106
107 The selected aerodynamic fallout samples range in diameter from 1.3-2.4 mm and in mass from 2.5-14.5 mg (Table
108 1). They appear light to dark green in color and are optically translucent and glossy. Vesicles are visible within the
109 volume of some of the glasses.

110
111 *[Table 1 — Fallout spherule labels, masses, and average diameters.]*

112 113 **2.2 Experimental methods**

114 **2.2.1 SEM, EDS, and EPMA**

115 Backscattered electron images of the samples were taken using an FEI Inspect-F SEM equipped with an AMETEK
116 EDAX Apollo XL Si drift energy-dispersive x-ray spectrometer. The SEM was operated at an accelerating voltage
117 of 20 kV with a beam current of ~1.5 nA.

118 Elemental maps and major element compositions were determined with a JEOL JXA-8200 electron probe equipped
119 with five wavelength-dispersive spectrometers, and a JEOL energy-dispersive x-ray spectrometer. X-ray intensities
120 were converted to concentrations using CITZAF (Armstrong, 1995). The EPMA was operated with a 15 kV
121 accelerating potential, 5 nA of probe current and a 2 μm beam diameter. The following silicate and oxide standards
122 were used: orthoclase (for Si, Al, K), Fe_2O_3 (for Fe), spessartine (for Mn), rutile (for Ti), diopside (for Ca), albite
123 (for Na), and MgO (for Mg). The samples were analyzed for major element composition in rectangular arrays with
124 30-100 spot analyses per sample. Regions adjacent to vesicles, cracks or pits that resulted in element concentrations
125 of less than 98 wt.% or greater than 102 wt.% were excluded from our data set.

126 127 **2.2.2 Sample autoradiography**

128 To obtain the autoradiographs, the samples were placed onto a photo-phosphor imaging plate for 34 hours inside a
129 light-blocking tent. All five samples were imaged together on the same plate for the same length of time, to provide
130 relative qualitative images of activity distributions. The plate was developed and the autoradiograph images
131 digitized using a GE Typhoon 7000 scanner at a spatial resolution of 50 $\mu\text{m}/\text{pixel}$. The autoradiographs record the
132 distributions of β^- activity and near-surface α activity (respective mean free paths of ~1 cm and ~10 μm in silicates).
133 Autoradiographs of these samples are dominated by β^- activity because of the low specific activity of U in these
134 samples. The fission products ^{137}Cs and ^{90}Sr are the dominant sources of β^- radioactivity in fallout samples more
135 than several decades old, and are likely the major contributors of β^- radioactivity in these samples.

136 137 **2.2.3 Spatially-resolved U isotope measurements**

138 Spatially-resolved U isotope ratios were measured by SIMS in two separate analytical sessions, one at Lawrence
139 Livermore National Laboratory (LLNL) using a modified Cameca ims-3f SIMS instrument to analyze four of the
140 five spherules (U1A was not analyzed at LLNL), and one at Los Alamos National Laboratory (LANL) using a
141 Cameca ims-1280 SIMS to analyze all five spherules. The LLNL analyses measured the $^{235}\text{U}/^{238}\text{U}$ ratio on four
142 spherules and U concentrations on two spherules (U3 and U4), while the LANL analyses measured the $^{234}\text{U}/^{238}\text{U}$,

143 $^{235}\text{U}/^{238}\text{U}$, and $^{236}\text{U}/^{238}\text{U}$ ratios on all five spherules. Approximately 20 spot analyses were performed per spherule at
144 LLNL, and between 3 and 45 spot analyses were performed per sample at LANL (Fig. 2).

145 SIMS analyses at LLNL were conducted using a 5 nA, $^{16}\text{O}^-$ primary ion beam that impacted the sample with a
146 kinetic energy of 17 keV, focused into a spot of ~10-30 μm diameter. Positive secondary ions were accelerated to
147 4500 V and focused into the mass spectrometer set to a mass resolving power of ~3000, sufficient to resolve the
148 relevant molecular interferences, and were then counted using a single electron multiplier detector. Data were
149 collected using two different mass sequences. Initially, data were obtained for masses 250.8 (used for background
150 signal characterization), 251 ($^{235}\text{U}^{16}\text{O}^+$), and 254 ($^{238}\text{U}^{16}\text{O}^+$); the intensities of $^{234}\text{U}^{16}\text{O}^+$ and $^{236}\text{U}^{16}\text{O}^+$ were below the
151 detection limits of the instrument. In a second series of analyses, the mass table was expanded to include mass 29.8
152 (background) and 30 ($^{30}\text{Si}^+$), such that the U concentration at each analysis spot could be determined through
153 comparison of the spherule's average Si concentration (determined by EPMA) and ($^{235}\text{U}^{16}\text{O}^+ + ^{238}\text{U}^{16}\text{O}^+$)/ $^{30}\text{Si}^+$ ratio to
154 the same ratio and nominal glass composition in our ~350 $\mu\text{g}/\text{g}$ U-bearing glass standard. SIMS analyses in
155 locations where the Si concentration deviated significantly ($>2\sigma$) from the average Si concentration of the spherule
156 were excluded from the U concentration calculations.

157 At LLNL, a single SIMS analysis consisted of 70-100 cycles, where for each cycle, the magnetic field was adjusted
158 to each of the analyzed masses for a user-defined period of time. A single cycle took approximately 30 seconds.
159 Each cycle, the uranium masses were counted for 3-5 s, with typical count rates of 100-300 counts per second on
160 $^{235}\text{U}^{16}\text{O}^+$. When we measured $^{30}\text{Si}^+$ (on spherules U3 and U4), typical count rates were 200,000-300,000 counts per
161 second. Magnet settling times depend on the applied change in the magnetic field, but were typically on the order of
162 ~1 s.

163

164 *[Figure 2 - Backscattered electron images with SIMS analysis locations overlaid. The contrast of*
165 *each image was individually adjusted to emphasize compositional zoning features and no*
166 *inferences about compositional differences between the samples should be drawn from these*
167 *images. Filled blue circles show the locations of the LLNL SIMS analyses (spot size: ~10-30 μm),*
168 *while filled yellow squares show the locations of the LANL SIMS analyses (raster size: 25 x 25*
169 *μm). The markers have been enlarged to ease viewing and are not representative of the actual size*
170 *of the SIMS analyses. Sample U1B is shown twice, as this sample was initially analyzed at LLNL,*
171 *then re-polished to expose a different surface, prior to analysis at LANL.]*

172

173 SIMS analyses at LANL were conducted using a 20-30 nA $^{16}\text{O}^-$ primary ion beam that impacted the sample with a
174 kinetic energy of 20 keV. Positive secondary ions were accelerated to 10 kV and detected using either mono-
175 collection (magnetic peak switching with a single electron multiplier detector) or multi-collection (static magnetic
176 field with multiple electron multiplier detectors). The ion transfer optics were tuned to image an 80 μm field of view
177 using a 400 μm diameter contrast aperture and a 3000-4000 μm diameter field aperture. A mass resolving power of
178 ~3000-4000 was used for both the mono-collector and the multi-collector analyses. Nuclear magnetic resonance
179 control was used to stabilize the magnet for analyses performed by static multi-collection. A 40 x 40 μm area was
180 pre-sputtered for 60 seconds, after which secondary ions were collected from a 25 x 25 μm rastered area for the
181 mass sequence 233.8 (used for background signal characterization), $^{234}\text{U}^+$, $^{235}\text{U}^+$, $^{236}\text{U}^+$, and $^{238}\text{U}^+$.

182 At LANL, spherules U1A, U1B, U2, and U3 were analyzed in mono-collection mode and spherule U4 was analyzed
183 in multi-collection mode. In mono-collection, a single analysis consisted of 20-25 cycles, where cycles took
184 approximately 30 seconds. For each cycle, the uranium masses were counted for between 2-5 s, with typical count
185 rates of 2000-5000 counts per second on $^{235}\text{U}^+$. The magnet was settled for 1 s between masses. In multi-collection,
186 data were collected in 2 second cycles for 50 cycles, with typical count rates of ~1700 counts per second on $^{235}\text{U}^+$.

187 The accuracy, precision, and instrumental mass fractionation of U isotope analyses made at LLNL and LANL were
188 determined using two synthetic silicate glasses doped respectively with ~350 $\mu\text{g}/\text{g}$ and ~3,500 $\mu\text{g}/\text{g}$ of uranium,
189 fabricated following the procedure outlined in Appendix A. Multi-collector inductively-coupled plasma mass
190 spectrometry (MC-ICP-MS) was used to measure the U concentration and U-isotope composition of the glasses
191 following procedures discussed in Appendix A; the results are shown in Table 2.

192

193 *[Table 2 – U Concentrations and U isotopic ratios of our U-bearing glass standards as measured*

194 *by MC-ICP-MS.]*

195
196 The standards were measured periodically throughout the analytical sessions to correct for any day-to-day variability
197 in the mass bias of the SIMS instruments. We measured the ~350 µg/g standard 23 times at LLNL and measured the
198 ~3,500 µg/g standard 10 times at LANL while operating the instrument as a multi-collector and 7 times while
199 operating as a mono-collector (Appendix A). We present the accuracy as the percent deviation of the mean of the
200 SIMS measurements from measurements made with MC-ICP-MS (Table 2) and precision as two times the relative
201 standard error of the mean (Table 3). The lower precision and accuracy of the multi-collector analyses of the
202 $^{234}\text{U}/^{238}\text{U}$ and $^{236}\text{U}/^{238}\text{U}$ ratios reflects differences in the experimental protocol, which led to poorer counting
203 statistics for $^{234}\text{U}^+$ and $^{236}\text{U}^+$.

204
205 *[Table 3 - Accuracy and precision of the SIMS measurements on our U-bearing glass standards.]*

206

207 **3. Results**

208 **3.1 Distribution of major elements and radionuclides**

209 The backscattered electron images and quantitative EPMA compositional maps show that spherules U1A and U1B
210 are nearly circular in cross section and free of large internal variations in chemical composition (Figs. 2 and 3). The
211 polished section of U1A contains several large (10-100s of µm in diameter) vesicles, while U1B is nearly void-free
212 in cross-section. The regions appearing dark in the backscattered electron images and bright in the Si compositional
213 maps of U1A and U1B consist entirely of Si and O, determined using EDS, and are likely quartz that was partially
214 or completely melted during detonation. Sample U2 has an elongated, teardrop shape with one large vesicle and
215 multiple smaller vesicles, and exhibits greater compositional heterogeneity than the four other samples. U3 is ~2.4
216 mm in maximum diameter and semi-circular in cross section with many vesicles clustered near the center, exhibiting
217 some Ca heterogeneity and several enriched Si regions that have sharply delineated boundaries (Fig. 3). U4 is ~2.3
218 mm in maximum diameter and also semi-circular in cross section, with no significant voids. Like U2, sample U4
219 appears to exhibit larger scale compositional heterogeneity, particularly with respect to Ca (Fig. 3).

220

221 *[Figure 3 – Chemical compositional maps for all 5 spherules. Composition maps of Si, Al, Ca,*
222 *and Fe (respectively) determined from wavelength-dispersive x-ray spectrometry mapping using*
223 *EPMA. All scale bars are 500 µm.]*

224

225 Nine oxides account for ~99% of the composition of the spherules (because the spherule major element bulk
226 compositions are similar to that of the local soils (see Eppich et al, 2014), we assume major elements are present in
227 their oxide forms). The results of the EPMA analyses (Table 4) indicate that all five samples have similar major
228 element chemical compositions, enriched in Si (~72% SiO₂) and Al (~14% Al₂O₃). Two samples, U2 and U4, have
229 regions characterized by two distinct compositional regions, indicated by the bright and dark regions in the
230 respective backscattered electron images, and highlighted in the Ca compositional maps (Figs. 2 and 3). The relative
231 standard deviation (the standard deviation divided by the mean) of the CaO concentration illustrates a difference of
232 7.5% for U1A versus 55% for U2 and 30% for U4. For U2, the CaO, FeO, K₂O, and MgO concentrations are
233 significantly different (>2σ) between the bright and dark regions in the backscattered electron image and Ca
234 compositional map (the bright region is enriched in CaO, FeO, and MgO and depleted in K₂O relative to the dark
235 region). For U4, CaO, Al₂O₃, and SiO₂ concentrations are significantly different between the two regions (the bright
236 region is enriched in CaO and Al₂O₃ and depleted in SiO₂ relative to the dark region).

237

238 *[Table 4 – Average major element compositions in wt.% of multiple EPMA spot analyses for all 5*
239 *spherules. The 1σ symbols refer to one standard deviation of multiple analyses.]*

240 *[Table 5 – Average major element compositions in wt.% of multiple EPMA spot analyses for*
241 *different compositional regions in spherules U2 and U4. Average major element compositions in*
242 *wt.% determined by EPMA for samples U2 and U4 separated into measurements made in the*

243 *bright and dark regions, as determined from the backscattered electron image and Ca*
244 *compositional map (Figs. 2 and 3). Measurements taken on the boundary of the regions were*
245 *discarded. The 1 σ symbols refer to one standard deviation of multiple analyses.]*

246

247 There are large differences in relative radioactivity between the five samples, with U1A exhibiting much lower
248 activity compared to U1B, which exhibits the highest activity (Fig. 4). In U1A and U1B, activity is homogeneously
249 distributed, while U2, U3, and U4 show heterogeneous activity distributions. In U2, the region of lowest activity
250 correlates with the region of lower average atomic number (Fig. 2), the region relatively depleted in CaO, FeO, K₂O,
251 and MgO (Fig. 3). Sample U4 exhibits the opposite correlation, however, with the region of lowest activity
252 correlating with the region of higher average atomic number (Figs. 2), relatively enriched in CaO and Al₂O₃ (Fig 3).

253

254 *[Figure 4 - Backscattered electron (top) and autoradiography (bottom) images of the 5 fallout*
255 *glasses characterized in this study. Backscattered electron micrographs show polished mid-*
256 *sections of the samples. The contrast of each image was individually adjusted to emphasize*
257 *compositional zoning features and no inferences about compositional differences between the*
258 *samples should be drawn from these images. The bright region towards the center of sample U3 is*
259 *sample charging. On the bottom, false color qualitative autoradiography images indicate both α*
260 *and β activity (but is likely dominated by β activity due to the low specific activity of uranium in*
261 *these samples), where yellow-white areas depict areas of highest activity. All five images were*
262 *obtained from the same exposure and differences in color reflect relative differences in*
263 *radioactivity within and between the samples. All scale bars are 500 μm .]*

264

265 3.2 Uranium isotope distributions

266 Combining analytical sessions at LLNL and LANL, we measured the ²³⁵U/²³⁸U ratio in 184 locations. Among all
267 five spherules, the ²³⁵U/²³⁸U isotope ratio spans a factor of nearly 600, from 0.02 to 11.84 (Table 6 and Fig. 5). The
268 lowest ²³⁵U/²³⁸U ratio (²³⁵U/²³⁸U=0.02) measured is ~2.75 times greater than that of natural uranium
269 (²³⁵U/²³⁸U=0.00725). The highest ²³⁵U/²³⁸U ratio falls below that of so-called oralloy (²³⁵U/²³⁸U~17.3, or ~93%
270 enriched in ²³⁵U), a type of highly enriched uranium common in the U.S. nuclear stockpile during the era of above
271 ground testing (Moody, 1994). Within a single spherule, U2, the ²³⁵U/²³⁸U ratio ranges from 0.02 to 7.41, a factor of
272 nearly 400 (Fig. 5). In MC-ICP-MS analyses of whole spherules, similar variation has been observed, but to a far
273 lesser degree (from ²³⁵U/²³⁸U=2.32 to ²³⁵U/²³⁸U=7.72 in 28 samples; Eppich et al., 2014).

274 The 104 SIMS analyses made at LANL also measured the ²³⁴U/²³⁸U and ²³⁶U/²³⁸U ratios. These minor isotope ratios
275 also span a large range of values, from ²³⁴U/²³⁸U=0.0003 and ²³⁶U/²³⁸U=0.0002 in one analysis on spherule U2 to
276 ²³⁴U/²³⁸U=0.09 and ²³⁶U/²³⁸U=0.04 in one analysis on spherule U1B (Figs. 6 and 7; Table 6). In addition, the minor
277 U isotope ratios show a strong linear correlation among all five samples when plotted against ²³⁵U/²³⁸U (Figs. 6 and
278 7). For ²³⁴U/²³⁸U vs. ²³⁵U/²³⁸U, a linear fit to the data has a slope and 2 σ uncertainty of 0.01082 \pm 0.00007 (R² =
279 0.999). For ²³⁶U/²³⁸U vs. ²³⁵U/²³⁸U, a linear fit has a slope and 2 σ uncertainty of 0.00479 \pm 0.00005 (R² = 0.997).
280 Both fits have y-intercepts that pass through the origin within 2 σ uncertainties.

281

282 *[Table 6 – SIMS measurements of U isotope ratios on all 5 spherules. Uncertainties are 2 σ .]*

283

284 Samples U1A and U1B are relatively homogeneous with respect to both chemical composition (Table 1 and Fig. 3)
285 and uranium isotope ratios, except for the single ²³⁵U/²³⁸U ratio of 11.84 measured near the periphery of U1B (Figs.
286 8 and 9). The three measurements on U1A have a mean ²³⁵U/²³⁸U ratio of 3.48 and relative standard deviation of
287 11.0%. For U1B, the mean value of the ²³⁵U/²³⁸U ratios (excluding the 11.84 value) is 7.14, with a relative standard
288 deviation of 8.3%. By comparison, samples U2, U3, and U4, yielded relative standard deviations in measured
289 ²³⁵U/²³⁸U ratios of 76.7%, 42.7%, and 26.4%, for U2, U3, and U4, respectively. We found no systematic variation in
290 the ²³⁵U/²³⁸U ratio with position in U1A and U1B, and our observations collectively show that these two samples are
291 relatively well mixed in both major elements and uranium isotopes.

292 As stated above, U1B exhibits a singularly high $^{235}\text{U}/^{238}\text{U}$ ratio of 11.84 near the spherule's periphery. We explored
293 the spatial extent of this region by translating the stage $\sim 20\ \mu\text{m}$ and performing another SIMS analysis. The
294 $^{235}\text{U}/^{238}\text{U}$ ratio in this second location is 8.16, indistinguishable from values measured elsewhere in the sample. This
295 observation suggests that at least this one localized U-isotope heterogeneity in U1B has a characteristic spatial scale
296 of $\sim 10\ \mu\text{m}$ or less.

297 U3 exhibits greater compositional (particularly with respect to Ca; Table 4 and Fig. 3) and U isotope heterogeneity
298 compared to U1A or U1B (Fig. 10). The relative standard deviations of the Ca concentration and $^{235}\text{U}/^{238}\text{U}$ ratios for
299 U3 are 20% and 43%, respectively (compared with U1A's respective relative standard deviations of 7.5% and
300 11.0%). The large relative standard deviation in the $^{235}\text{U}/^{238}\text{U}$ ratio in U3 reflects several low values near the center
301 of the sample, and reduces to 29% if those values are excluded. There are no features in the backscattered electron
302 image or composition maps with which these centrally located low ratios are correlated, but the autoradiography
303 image also shows a low activity region near the center of the sample (Fig. 4), suggesting that heterogeneous
304 distributions of trace constituents but not major element constituents may correlate with the observed variation in U
305 isotopes in sample U3.

306 Spherules U2 and U4 exhibit correlations between U isotope ratios and major element composition (Figs. 11 and
307 12). In U2, measured U-isotope ratios appear to correlate with two distinct compositional regions. One region,
308 characterized by $1 < ^{235}\text{U}/^{238}\text{U} < 8$, is enriched in CaO, FeO, and MgO (bright region in U2's Ca and Fe
309 compositional maps), while the second region, characterized by $0.02 < ^{235}\text{U}/^{238}\text{U} < 1$, is associated with the region
310 enriched in K_2O (dark regions in U2's Ca and Fe compositional maps; Table 5, Figs. 3 and 11). The $^{235}\text{U}/^{238}\text{U}$ ratios
311 in sample U4 also display this type of bimodal behavior. However, in contrast to sample U2, the regions enriched in
312 CaO in sample U4 are associated with *lower* $^{235}\text{U}/^{238}\text{U}$ ratios (Table 5, Figs. 3 and 12). The regions enriched in CaO
313 and Al_2O_3 (bright regions in the Ca compositional map for sample U4) contain $2 < ^{235}\text{U}/^{238}\text{U} < 4$, while the regions
314 enriched in SiO_2 and depleted in CaO and Al_2O_3 (dark regions in the Ca compositional map for sample U4) are
315 associated with higher $^{235}\text{U}/^{238}\text{U}$ ratios, $4 < ^{235}\text{U}/^{238}\text{U} < 6.5$ (Figs. 3 and 12).

316 In two of the samples, U3 and U4, the $^{235}\text{U}/^{238}\text{U}$ ratio and the uranium concentration were simultaneously measured
317 (Fig. 13 and Appendix B). Measured uranium concentrations range from 3 to 19 $\mu\text{g/g}$, with a 2σ uncertainty of 8-
318 15% (this uncertainty is dominated by the variability in the SiO_2 concentration in the spherules measured using
319 EPMA, as the SiO_2 concentration is assumed constant relative to changes in U concentration). In contrast, the
320 concentration of uranium in fallout-free soils near ground zero ranges from 2.7 to 4.8 $\mu\text{g/g}$, and bulk uranium
321 concentrations reported from single spherules ranged from 14.7 to 32.9 $\mu\text{g/g}$ (Eppich et al., 2014). Uranium
322 concentrations in U3 and U4 show strong positive correlations with the measured $^{235}\text{U}/^{238}\text{U}$ ratio ($R^2=0.77$ as a
323 combined data set with one outlier excluded; $R^2=0.68$ with the outlier included).

324

325 *[Figure 5 - Histogram of all $^{235}\text{U}/^{238}\text{U}$ measurements. There are 25 bins spaced equally between*
326 *$^{235}\text{U}/^{238}\text{U}=0.01$ and $^{235}\text{U}/^{238}\text{U}=20$. The preponderance of low $^{235}\text{U}/^{238}\text{U}$ ratios in U2, contrasted*
327 *with higher values in U1B and U4 is apparent. Data are from LANL and LLNL.]*

328 *[Figure 6 - Composite 3-isotope plot of $^{234}\text{U}/^{238}\text{U}$ vs. $^{235}\text{U}/^{238}\text{U}$ for all spherules. Uncertainties are*
329 *2σ . Data are from LANL.]*

330 *[Figure 7 Composite 3-isotope plot of $^{236}\text{U}/^{238}\text{U}$ vs. $^{235}\text{U}/^{238}\text{U}$ for all spherules. Uncertainties are*
331 *2σ . Data are from LANL.]*

332 *[Figure 8 - $^{235}\text{U}/^{238}\text{U}$ vs. distance from the spherule's center on U1A. Uncertainties are 2σ . Data*
333 *are from LANL.]*

334 *[Figure 9 - $^{235}\text{U}/^{238}\text{U}$ vs. distance from the spherule's center on U1B. Note the singularly high*
335 *$^{235}\text{U}/^{238}\text{U}$ ratio of 11.84 near the periphery. Uncertainties are 2σ . Data are from LANL and*
336 *LLNL.]*

337 *[Figure 10 - $^{235}\text{U}/^{238}\text{U}$ vs. distance from the spherule's center on U3. Uncertainties are 2σ . Data*
338 *are from LANL and LLNL.]*

339 *[Figure 11 - $^{235}\text{U}/^{238}\text{U}$ vs. distance from the spherule's center on U2. Note the logarithmic*
340 *ordinate scale. Data are separated into SIMS measurements taken in the bright and dark regions,*

341 *as defined in the text and shown in the backscattered electron image and Ca and Fe compositional*
342 *maps (Figs. 2 and 3). Uncertainties are 2σ . Data are from LANL and LLNL.]*

343 *[Figure 12 - $^{235}\text{U}/^{238}\text{U}$ vs. distance from the spherule's center on U4. Data are separated into*
344 *SIMS measurements taken in the bright and dark regions, as defined in the text and shown in the*
345 *backscattered electron image and Ca compositional map (Figs. 2 and 3). Uncertainties are 2σ .*
346 *Data are from LANL and LLNL.]*

347 *[Figure 13 - $^{235}\text{U}/^{238}\text{U}$ vs. uranium concentration for samples U3 and U4. The vertical bar*
348 *represents the range of U concentrations measured in five soil samples proximate to ground zero*
349 *(between 2.7 and 4.8 $\mu\text{g/g}$; Eppich et al., 2014). Uncertainties are 2σ . Data are from LLNL.]*

350

351 **4. Discussion**

352 **4.1 Compositional heterogeneity and fallout formation processes**

353 Our results suggest that the scale uranium isotope heterogeneity observed within aerodynamic glassy fallout
354 spherules is even greater than that revealed (e.g., Eppich et al., 2014) through studies of whole spherules. In a single
355 spherule, U2, the U isotopic ratio varies by nearly a factor of 400, while in another single spherule, U1B (if the
356 outlier of 11.84 is excluded) the U isotopic ratio varies by less than 10%. Heterogeneity in U concentration also
357 varies greatly from sample to sample, and within individual samples of aerodynamic glassy fallout. Spatial analyses
358 make it clear that the elevated concentration of uranium observed in aerodynamic glasses correlates with, and is
359 derived from, contributions from the device. Previously reported U concentrations from single spherules (15 to 33
360 $\mu\text{g/g}$; Eppich et al., 2014) overlap our observed range of U concentrations within spherules (3 to 19 $\mu\text{g/g}$), but the
361 former are systematically higher. It remains unclear if this difference is due to our limited sample size (spatial
362 concentration measurements were obtained in select SIMS analyses and from a subset of two samples). As
363 demonstrated by U isotope measurements, however, it is expected that the degree of chemical heterogeneity
364 observed in such samples can be dampened through application of bulk measurement techniques. We anticipate that
365 if additional spatial analyses of U concentration are pursued, we will observe and likely surpass the concentration
366 values reported from bulk measurements.

367 The degree of uranium isotope heterogeneity, major element compositions reflecting a dominant contribution from
368 nearby soils, and physical sample dimensions do not support agglomeration of pure vapor condensates as a primary
369 mechanism in forming fallout of the type analyzed for this study. The compositional and U isotopic variation
370 observed in samples U2 and U4, for example suggests these spherules formed through the collision and mixing of
371 two or more relatively large, molten objects of dissimilar, but aluminosilicate-dominated composition. As can be
372 seen in the compositional maps, two distinct compositional regions are defined in both U2 and U4 (Figs. 2 and 3).
373 Each of those regions is also bimodal with respect to U isotope compositions. Such evidence implies that the melts
374 forming these two regions must have incorporated different amounts of U from the device prior to agglomeration
375 and partial mixing. The final agglomerated objects experienced little mixing before fusing, preserving these textures.
376 Of note, while both U2 and U4 reveal a correlation between CaO concentration and U isotope composition, the
377 samples are correlated in opposing senses. Spherule U2 shows a negative correlation, whereas spherule U4 shows a
378 positive correlation. Generally, Ca is regarded as a more refractory species, while U tends towards more volatile
379 behavior (Miller, 1960; Bedford and Jackson, 1965). Such opposing observations in fallout from the same event
380 makes it clear that in the case of this particular test, formation conditions favored multiple chemical behaviors.
381 Understanding the physical and chemical processes that result in such dichotomy will require additional study.

382 A distinguishing feature in two other spherules, U1A and U1B, is the relative homogeneity of U isotope composition
383 and major element compositions within the spherules. We interpret this to mean that the molten precursor droplets
384 were held above the solidification temperature (~ 1300 K, determined by MELTS calculations of liquidus
385 temperatures for glasses of these compositions; Ghiorso and Sack, 1995; Asimow and Ghiorso, 1998) long enough
386 at high enough temperature to effectively homogenize the silicate melts. This may have occurred through a
387 combination of convective and/or diffusive processes, but the present study cannot differentiate between the two.
388 Alternatively, such spherules may have formed by agglomeration of parcels of melt that were similar with respect to
389 composition and U isotopic composition.

390

391 **4.2 Mixing between natural and enriched uranium**

392 The observed range of U isotope ratios in the spherules provides evidence for mixing between at least two sources of
 393 uranium with different isotopic compositions. As previously stated, the maximum observed $^{235}\text{U}/^{238}\text{U}$ ratio in this
 394 study, 11.84 (~91.5% enriched in ^{235}U , assuming 1% ^{234}U), approaches the $^{235}\text{U}/^{238}\text{U}$ ratio in oralloy
 395 ($^{235}\text{U}/^{238}\text{U}\sim 17.3$), while the minimum measured $^{235}\text{U}/^{238}\text{U}$ ratio, ~0.02 in sample U2, approaches the $^{235}\text{U}/^{238}\text{U}$ value
 396 found in natural uranium, $^{235}\text{U}/^{238}\text{U}=0.00725$. The correlated variations in the minor isotope ratios, $^{234}\text{U}/^{238}\text{U}$ and
 397 $^{236}\text{U}/^{238}\text{U}$, are also consistent with values approaching these two end-members. Using natural uranium and oralloy as
 398 end-members, we calculate the relative contribution of each end-member to each $^{235}\text{U}/^{238}\text{U}$ isotopic ratio
 399 measurement, assuming simple two component mixing. This calculation assumes (1), the only source of enriched
 400 uranium is represented by oralloy from the device and (2), isotopic fractionation of uranium in the silicate melt can
 401 be neglected. To a good approximation, we may ignore the minor isotopes in natural uranium, as ^{234}U only
 402 ~0.0055% of natural uranium, and the ^{236}U content in natural uranium is vanishingly small (Richter et al., 1999).

403 With these assumptions, let the isotopic abundances of ^{235}U and ^{238}U in natural uranium be represented as $y_{235} =$
 404 0.00725 and $y_{238} = 0.99275$. Similarly, let x_{235} and x_{238} represent the abundances of ^{235}U and ^{238}U in the enriched
 405 uranium end-member. Let n_f and n_n represent, respectively, the contributions from the enriched and natural uranium
 406 end-members in an individual SIMS measurement. The number of atoms of ^{235}U and ^{238}U in an individual
 407 measurement is given by:

408
$$^{235}\text{U}: n_{235} = n_f x_{235} + n_n y_{235}, \tag{1a}$$

409
$$^{238}\text{U}: n_{238} = n_f x_{238} + n_n y_{238}. \tag{1b}$$

410

411 The $^{235}\text{U}/^{238}\text{U}$ ratio may then be represented as:

412
$$\frac{n_{235}}{n_{238}} = \frac{n_f x_{235} + n_n y_{235}}{n_f x_{238} + n_n y_{238}}. \tag{2}$$

413 Solving Equation 2 for n_n/n_f gives an expression of the relative contribution from the two uranium isotope end-
 414 members to each U isotope ratio:

415
$$\frac{n_n}{n_f} = \frac{x_{235} - \frac{n_{235}}{n_{238}} x_{238}}{\frac{n_{235}}{n_{238}} y_{238} - y_{235}}. \tag{3}$$

416 Equation 3, using our measurements, is plotted in Figure 14, illustrating the range of mixing observed between the
 417 uranium isotope end-members assumed in this model.

418

419 *[Figure 14 - Ratio of natural to enriched U for each SIMS analysis. Contributions of uranium of*
 420 *natural isotopic composition (n_n) relative to uranium from the enriched (HEU) end-member (n_f) as*
 421 *a function of the $^{235}\text{U}/^{238}\text{U}$ ratio for samples U1A, U1B, U2, U3, and U4, calculated from Equation*
 422 *3. The dashed line represents the solution to Equation 3 and depicts the shape of the mixing line.*
 423 *The mixing line asymptotically approaches infinity as the $^{235}\text{U}/^{238}\text{U}$ ratio approaches the*
 424 *composition of natural uranium, $^{235}\text{U}/^{238}\text{U} = 0.00725$, and asymptotically approaches zero as the*
 425 *$^{235}\text{U}/^{238}\text{U}$ ratio approaches 17.3, the $^{235}\text{U}/^{238}\text{U}$ ratio in oralloy (Moody, 1994). Where uncertainties*
 426 *(2σ) are not visible, they are smaller than the data points.]*

427

428 **5. Conclusions**

429 Five fallout spherules were characterized using SIMS, SEM/EDS, EPMA, and autoradiography. Two samples (U1A
 430 and U1B) are far more relatively homogenous with respect to both major element composition and uranium isotopes
 431 than the other three (U2, U3, and U4), suggesting these objects had longer residence times within the fireball at high
 432 temperature, or were formed from approximately homogenous precursors, with respect to composition and uranium

433 isotopes. The $^{235}\text{U}/^{238}\text{U}$ ratio is correlated with major element composition in two spherules, suggesting
434 agglomeration of molten or partially molten precursors, followed by rapid cooling.

435 Individual spherules display variable compositional heterogeneity suggestive of rapid cooling and incomplete
436 mixing, exhibiting heterogeneity in U isotopes with $0.02 < ^{235}\text{U}/^{238}\text{U} < 11.84$ among the five spherules, and $0.02 <$
437 $^{235}\text{U}/^{238}\text{U} < 7.84$ within a single spherule. Correlated variations among the $^{234}\text{U}/^{238}\text{U}$, $^{235}\text{U}/^{238}\text{U}$, and $^{236}\text{U}/^{238}\text{U}$ ratios
438 point to mixing between end-member components corresponding to highly enriched uranium derived from the
439 device and natural uranium. The range of heterogeneity in measured uranium isotope ratios suggests that these
440 spherules preserve a mixture of uranium from at least two end-members with distinct uranium isotope compositions.
441 We used a two-component mixing model, one end-member being natural uranium and the other having the
442 composition of oralloy (HEU), to illustrate the range of mixing between natural and enriched U in these fallout
443 glasses.

444 The extent of mixing and the magnitude of uranium isotopic heterogeneity provide important constraints on the
445 thermal history of aerodynamic fallout glasses, showing that both agglomeration and molten mixing of chemically
446 heterogeneous molten precursor materials must have been key formation processes prior to quenching. These studies
447 suggest preservation of millimeter to micron scale chemical heterogeneities in the fireball over time scales of
448 seconds, and point the way to developing a more quantitative understanding of the formation of fallout.

449

450 **Acknowledgments**

451 We dedicate this paper to the memory of Ian D. Hutcheon, who served not only as mentor, colleague, and friend, but
452 also as a source of unparalleled inspiration to us all.

453 We thank Christina Ramon for help with sample preparation; Ross Williams, Kerri Schorzman, and Darren
454 Tollstrup for MC-ICP-MS measurements of the standard glasses; Gary Eppich, Ben Jacobsen, and Naomi Marks for
455 helpful discussions; and Gary Stone and Anna Lindquist for assistance with autoradiography. This research was
456 performed under appointment to the Nuclear Nonproliferation International Safeguards Graduate Fellowship
457 Program sponsored by the National Nuclear Security Administration's Next Generation Safeguards Initiative. This
458 work was supported by the Laboratory Directed Research and Development Program (project 10-SI-016) at LLNL
459 and the NNSA Office of Defense Nuclear Nonproliferation Research and Development and performed under the
460 auspices of the U.S. Department of Energy by Lawrence Livermore National Laboratory under Contract DE-AC52-
461 07NA27344.

462

463 **References**

- 464 Adams, C. E., & O'Connor, J. D. (1957). *The nature of individual radioactive particles VI. Fallout particles from a*
465 *tower shot, Operation Redwing*. No. USNRDL-TR-208. U.S. Naval Radiological Defense Lab., San
466 Francisco, CA (United States).
- 467 Adams, C. E., Farlow, N. H., & Schell, W. R. (1960). The compositions, structures and origins of radioactive fall-
468 out particles. *Geochimica et Cosmochimica Acta*, 18(1), 42-56.
- 469 Asimow, P. D., & Ghiorso, M. S. (1998). Algorithmic modifications extending MELTS to calculate subsolidus
470 phase relations. *American Mineralogist*, 83, 1127-1132.
- 471 Armstrong, J. T. (1995). CITZAF – A package of correction programs for the quantitative electron microbeam x-
472 ray analysis of thick polished materials, thin films, and particles. *Microbeam Analysis*, 4(3), 177-200.
- 473 Bedford, R. G., Jackson, D. D. (1965). *Volatilities of the fission product and uranium oxides*. No. UCRL-12314.
474 Lawrence Radiation Lab., Livermore, CA (United States).
- 475 Belloni, F., Himbert, J., Marzocchi, O., & Romanello, V. (2011). Investigating incorporation and distribution of
476 radionuclides in trinitite. *Journal of Environmental Radioactivity*, 102(9), 852-862.
- 477 Bellucci, J. J., & Simonetti, A. (2012). Nuclear forensics: searching for nuclear device debris in trinitite-hosted
478 inclusions. *Journal of Radioanalytical and Nuclear Chemistry*, 293(1), 313-319.
- 479 Bellucci, J. J., Simonetti, A., Wallace, C., Koeman, E. C., & Burns, P. C. (2013). Isotopic fingerprinting of the
480 world's first nuclear device using post-detonation materials. *Analytical Chemistry*, 85(8), 4195-4198.
- 481 Bellucci, J. J., Simonetti, A., Koeman, E. C., Wallace, C., & Burns, P. C. (2014). A detailed geochemical
482 investigation of post-nuclear detonation trinitite glass at high spatial resolution: Delineating anthropogenic
483 vs. natural components. *Chemical Geology*, 365, 69-86.
- 484 Brode, H. L. (1968). Review of nuclear weapons effects. *Annual Review of Nuclear Science*, 18(1), 153-202.
- 485 Cassata, W. S., Prussin, S. G., Knight, K. B., Hutcheon, I. D., Isselhardt, B. H., & Renne, P. R. (2014). When the
486 dust settles: stable xenon isotope constraints on the formation of nuclear fallout. *Journal of Environmental*
487 *Radioactivity*, 137, 88-95.
- 488 Crocker, G. R., O'Connor, J. D., & Freiling, E. C. (1965). *Physical and radiochemical properties of fallout particles*.
489 No. USNRDL-TR-899. U.S. Naval Radiological Defense Lab., San Francisco, CA (United States).
- 490 Eby, N., Hermes, R., Charnley, N., & Smoliga, J. A. (2010). Trinitite—the atomic rock. *Geology Today*, 26(5), 180-
491 185.
- 492 Eppich, G. R., Knight, K. B., Jacomb-Hood, T. W., Spriggs, G. D., & Hutcheon, I. D. (2014). Constraints on fallout
493 melt glass formation from a near-surface nuclear test. *Journal of Radioanalytical and Nuclear Chemistry*,
494 1-17.
- 495 Fahey, A. J., Zeissler, C. J., Newbury, D. E., Davis, J., & Lindstrom, R. M. (2010). Post-detonation nuclear debris
496 for attribution. *Proceedings of the National Academy of Sciences*, 107(47), 20207-20212.
- 497 Glasstone, S., & Dolan, P. J. (1977). *The Effects of Nuclear Weapons*. US Department of Defense & US Department
498 of Energy.
- 499 Ghiorso, M. S., & Sack, R. O. (1995). Chemical mass transfer in magmatic processes IV. A revised and internally
500 consistent thermodynamic model for the interpolation and extrapolation of liquid-solid equilibria in
501 magmatic systems at elevated temperatures and pressures. *Contributions to Mineralogy and Petrology*, 119
502 (2-3), 197-212.
- 503 Hermes, R. E. & Strickfaden, W. B. (2005). A new look at trinitite. *Nuclear Weapons Journal*, 2, 2-7.
- 504 Izrael, Y. A. (2002). *Radioactive Fallout after Nuclear Explosions and Accidents*. Elsevier.
- 505 Mackin, J. L., Zigman, P. E., Love, D. L., MacDonald, D., Sam, D. (1958). *Radiochemical analysis of individual*
506 *fallout particles*. No. USNRDL-TR-386. U.S. Naval Radiological Defense Lab., San Francisco, CA
507 (United States).

508 Miller, C. F. (1960). *A theory of formation of fallout from land-surface nuclear detonations and decay of the fission*
509 *products*. No. USNRDL-TR-208. U.S. Naval Radiological Defense Lab., San Francisco, CA (United
510 States).

511 Miller, C. F. (1964). *Biological and radiological effects of fallout from nuclear explosions*. No. IMU-4536. Stanford
512 Research Institute, Menlo Park, CA (United States).

513 Moody, K.J. (1994). *Dissolved or alloy standards and the origin of HEU*. No. UCRL-ID-117611. Lawrence
514 Livermore National Lab., Livermore, CA (United States).

515 Parekh, P. P., Semkow, T. M., Torres, M. A., Haines, D. K., Cooper, J. M., Rosenberg, P. M., & Kitto, M. E. (2006).
516 Radioactivity in trinitite six decades later. *Journal of Environmental Radioactivity*, 85(1), 103-120.

517 Sharp, N., McDonough, W. F., Ticknor, B. W., Ash, R. D., Piccoli, P. M., & Borg, D. T. (2014). Rapid analysis of
518 trinitite with nuclear forensic applications for post-detonation material analyses. *Journal of Radioanalytical*
519 *and Nuclear Chemistry*, 302(1), 57-67.

520 Stewart, K. (1956). The condensation of a vapour to an assembly of droplets or particles. *Trans. Faraday Soc.*, 52,
521 161-173.

522 Tompkins, R. C., Russell, I. J., & Nathans, M. W. (1970). *Comparison between cloud samples and close-in ground*
523 *fallout samples from nuclear ground bursts*. Army Ballistic Research Lab., Aberdeen Proving Ground, Md
524 (United States).

525 Wallace, C., Bellucci, J. J., Simonetti, A., Hainley, T., Koeman, E. C., & Burns, P. C. (2013). A multi-method
526 approach for determination of radionuclide distribution in trinitite. *Journal of Radioanalytical and Nuclear*
527 *Chemistry*, 298(2), 993-1003.

528 Williams, R.W., Gaffney A.M. (2011). ^{230}Th - ^{234}U model ages of some uranium standard reference materials. *Proc.*
529 *Radiochemica Acta*, 1, 31-35.

530

531

532

533

534

535

536

537

538

539

540

541

542

543

544

545

546

547 Appendix A - Fabrication and measurements of U-bearing standard glasses

548 A.1 Fabrication of the U-bearing standard glasses

549 The standard glasses were prepared by doping a base glass composition corresponding to one of the eutectic
550 compositions in the CaO-Al₂O₃-SiO₂ system. The nominal composition is SiO₂=62 wt.%, Al₂O₃=14.5 wt.% and
551 CaO= 23.5 wt.%. This composition has a melting temperature of 1170°C. The base glass composition was prepared
552 from reagent grade SiO₂, Al₂O₃, and CaCO₃. The oxide-carbonate mix was ground under ethanol in an automated
553 agate mortar and pestle for 60 minutes and then dried under a heat lamp. The mix was then calcined in a platinum
554 crucible in air at 850°C overnight to decompose the CaCO₃. The calcine was then ground under ethanol in an
555 automated agate mortar and pestle for 60 minutes and then dried under a heat lamp. Finally, the base glass calcine
556 was fused in a bottom-loading Deltech furnace in a platinum crucible for a minimum of 8 hours at 1450°C and
557 quenched in water, producing a clear glass. The glass was then crushed in a hardened steel mortar and pestle, and
558 then ground under ethanol in an automated agate mortar and pestle for 60 minutes. This fusion-grinding procedure
559 was repeated two additional times.

560 The U-doped glasses were prepared by adding nitrate solutions containing 10,000 ppm of certified reference
561 material (CRM) U500 to the base glass to obtain glasses with uranium concentrations of ~500 and ~5,000 µg/g. The
562 solution was pipetted into ~5 g of the base glass for each of the glasses. Next, the mixture was ground by hand in a
563 fume hood under ethanol in an agate mortar and pestle for 60 minutes and dried.

564 Each mixture was fused in a bottom-loading Deltech furnace in a new platinum crucible for a minimum of 8 hours at
565 1450°C and quenched in water. A separate crucible was used for each concentration to minimize cross-
566 contamination. Following each fusion step, the glass was removed from the crucible and coarsely ground in a
567 hardened steel mortar. The coarse mix was then ground under ethanol in an agate mortar and pestle for 60 minutes
568 and dried. The fusion/grinding cycle was repeated a minimum of three times for each sample.

569 A.2 Isotopic and concentration measurements of the U-bearing standard glasses via MC-ICP-MS

570 The standard glasses were measured for U isotope ratios and U concentrations using a Nu Plasma I high resolution
571 MC-ICP-MS instrument. We used the U010 certified reference material for instrumental mass bias corrections. Each
572 glass was once for U isotopics and once, on a separately prepared aliquot using isotope dilution (spiked with ²³³U),
573 to obtain U concentrations.

574 The MC-ICP-MS measurements show that the glasses deviate from the desired concentrations of ~500 and ~5,000
575 µg/g of U and from the certified U isotope ratios of CRM U500 (Tables 2 and A1). The deviation of the U isotope
576 ratios in the U-bearing standard glasses from the CRM U500 dopant is likely due to U contamination during the
577 fabrication process.

578 *[Table A1: Deviations of U isotope ratios in LLNL and LANL standard glasses from CRM U500.*
579 *Uncertainties are 2σ.]*

580 A.3 SIMS measurements of the U-bearing standard glasses

581 *[Table A2: LLNL SIMS measurements of ²³⁵U/²³⁸U on the ~350 µg/g U-bearing glass standard.*
582 *Uncertainties are 2σ.]*

583 *[Table A3: LANL SIMS measurements of ²³⁴U/²³⁸U, ²³⁵U/²³⁸U, and ²³⁶U/²³⁸U on the ~3,500 µg/g*
584 *U-bearing glass standard. Modes refer to whether the instrument was operating as a mono-*
585 *collector or multi-collector. Uncertainties are 2σ.]*

586 Appendix B - U concentration data for spherules U3 and U4

587 *[Table B1: LLNL SIMS measurements of the U concentration and their corresponding ²³⁵U/²³⁸U*
588 *ratios for spherules U3 and U4. The first measurement on spherule U3 was excluded because the*
589 *composition of the analyzed region was highly enriched in Ca and highly depleted in Si,*
590 *invalidating the use of the (²³⁵U¹⁶O⁺ + ²³⁸U¹⁶O⁺)^{β0}Si⁺ ratio as a method to estimate the U*
591 *concentration in that location. Uncertainties are 2σ.]*

592 Table 1

Sample	Mass (mg)	Avg. Diameter (mm)
U1A	3.7	1.6
U1B	2.5	1.4
U2	4.5	1.6
U3	14.8	2.3
U4	14.4	2.2

593 Table 2

Standard	U Concentration ($\mu\text{g/g}$)			$^{235}\text{U}/^{238}\text{U}$			$^{234}\text{U}/^{238}\text{U}$			$^{236}\text{U}/^{238}\text{U}$		
		\pm	2σ		\pm	2σ		\pm	2σ		\pm	2σ
LLNL	359.1	\pm	1.2	0.9618	\pm	0.0013	0.010044	\pm	0.000006	0.001479	\pm	0.000006
LANL	3490	\pm	12	0.9949	\pm	0.0014	0.010371	\pm	0.000006	0.001521	\pm	0.000005

594 Table 3

Standard	Mode	# analyses	$^{235}\text{U}/^{238}\text{U}$		$^{234}\text{U}/^{238}\text{U}$		$^{236}\text{U}/^{238}\text{U}$	
			Accuracy (%)	Precision (%)	Accuracy (%)	Precision (%)	Accuracy (%)	Precision (%)
LLNL	mono	23	0.40	0.30	-	-	-	-
LANL	mono	7	1.06	0.17	1.62	0.22	1.03	0.49
LANL	multi	10	0.67	0.05	0.35	0.36	0.02	1.06

05 Table 4
 06

Sample	# pts	SiO ₂	1σ	Al ₂ O ₃	1σ	CaO	1σ	K ₂ O	1σ	Na ₂ O	1σ	FeO	1σ	TiO ₂	1σ	MnO	1σ	MgO	1σ	Sum
U1A	39	72.36 ± 1.35	14.56 ± 0.81	1.41 ± 0.18	3.69 ± 0.12	3.11 ± 0.15	3.67 ± 0.22	0.33 ± 0.02	0.13 ± 0.02	0.60 ± 0.06	99.86									
U1B	49	71.75 ± 0.74	14.49 ± 0.52	1.84 ± 0.14	3.64 ± 0.11	3.12 ± 0.10	3.44 ± 0.21	0.28 ± 0.03	0.09 ± 0.02	0.58 ± 0.04	99.23									
U2	48	72.18 ± 1.99	13.49 ± 1.25	1.10 ± 0.61	4.94 ± 0.53	3.72 ± 0.41	2.27 ± 0.83	0.23 ± 0.06	0.11 ± 0.03	0.38 ± 0.20	98.42									
U3	44	71.43 ± 1.67	13.65 ± 1.02	2.55 ± 0.51	3.87 ± 0.21	3.36 ± 0.22	3.27 ± 0.21	0.29 ± 0.03	0.15 ± 0.02	0.64 ± 0.06	99.21									
U4	49	71.90 ± 4.08	14.30 ± 2.27	2.61 ± 0.76	3.54 ± 0.54	2.97 ± 0.46	3.22 ± 0.50	0.29 ± 0.05	0.13 ± 0.03	0.56 ± 0.10	99.52									

597

598 Table 5

599

Sample	# pts	SiO ₂	1σ	Al ₂ O ₃	1σ	CaO	1σ	K ₂ O	1σ	FeO	1σ	MgO	1σ
U2 (bright)	14	70.93	± 1.38	13.34	± 1.20	1.79	± 0.19	4.44	± 0.21	3.20	± 0.27	0.59	± 0.07
U2 (dark)	13	72.83	± 0.92	14.06	± 0.61	0.45	± 0.24	5.50	± 0.29	1.36	± 0.22	0.16	± 0.07
U4 (bright)	13	69.59	± 0.59	15.54	± 0.40	3.37	± 0.14	3.44	± 0.06	3.18	± 0.10	0.58	± 0.02
U4 (dark)	17	72.51	± 1.02	13.96	± 0.56	2.14	± 0.39	3.71	± 0.28	3.37	± 0.26	0.58	± 0.06

Table 6

UIA	$^{235}\text{U}/^{238}\text{U}$	2σ	$^{234}\text{U}/^{238}\text{U}$	2σ	$^{236}\text{U}/^{238}\text{U}$	2σ	U2	$^{235}\text{U}/^{238}\text{U}$	2σ	$^{234}\text{U}/^{238}\text{U}$	2σ	$^{236}\text{U}/^{238}\text{U}$	2σ	U2 (cont.)	$^{235}\text{U}/^{238}\text{U}$	2σ	$^{234}\text{U}/^{238}\text{U}$	2σ	$^{236}\text{U}/^{238}\text{U}$	2σ
LANL-1	3.850 ± 0.064		0.0416 ± 0.0018		0.01822 ± 0.00111		LANL-1	3.372 ± 0.043		0.0360 ± 0.0016		0.01751 ± 0.00095		LANL-36	5.133 ± 0.043		0.0553 ± 0.0012		0.02482 ± 0.00082	
LANL-2	3.084 ± 0.051		0.0329 ± 0.0017		0.01538 ± 0.00110		LANL-2	3.841 ± 0.055		0.0416 ± 0.0014		0.01971 ± 0.00092		LANL-37	1.039 ± 0.026		0.0110 ± 0.0004		0.00483 ± 0.00034	
LANL-3	3.519 ± 0.074		0.0384 ± 0.0029		0.01886 ± 0.00151		LANL-3	2.178 ± 0.076		0.0239 ± 0.0011		0.01127 ± 0.00061		LANL-38	2.340 ± 0.023		0.0256 ± 0.0007		0.01114 ± 0.00044	
UIB	$^{235}\text{U}/^{238}\text{U}$	2σ	$^{234}\text{U}/^{238}\text{U}$	2σ	$^{236}\text{U}/^{238}\text{U}$	2σ	LANL-4 <th>$^{235}\text{U}/^{238}\text{U}$</th> <th>$2\sigma$</th> <th>$^{234}\text{U}/^{238}\text{U}$</th> <th>$2\sigma$</th> <th>$^{236}\text{U}/^{238}\text{U}$</th> <th>$2\sigma$</th> <th>LANL-39 <th>$^{235}\text{U}/^{238}\text{U}$</th> <th>$2\sigma$</th> <th>$^{234}\text{U}/^{238}\text{U}$</th> <th>$2\sigma$</th> <th>$^{236}\text{U}/^{238}\text{U}$</th> <th>$2\sigma$</th> </th>	$^{235}\text{U}/^{238}\text{U}$	2σ	$^{234}\text{U}/^{238}\text{U}$	2σ	$^{236}\text{U}/^{238}\text{U}$	2σ	LANL-39 <th>$^{235}\text{U}/^{238}\text{U}$</th> <th>$2\sigma$</th> <th>$^{234}\text{U}/^{238}\text{U}$</th> <th>$2\sigma$</th> <th>$^{236}\text{U}/^{238}\text{U}$</th> <th>$2\sigma$</th>	$^{235}\text{U}/^{238}\text{U}$	2σ	$^{234}\text{U}/^{238}\text{U}$	2σ	$^{236}\text{U}/^{238}\text{U}$	2σ
LANL - 1	7.609 ± 0.103		0.0836 ± 0.0025		0.03564 ± 0.00171		LANL-4	1.220 ± 0.011		0.0131 ± 0.0005		0.00615 ± 0.00033		LANL-39	2.390 ± 0.038		0.0253 ± 0.0008		0.01172 ± 0.00050	
LANL - 2	7.339 ± 0.092		0.0795 ± 0.0023		0.03476 ± 0.00141		LANL-5	3.187 ± 0.029		0.0346 ± 0.0009		0.01644 ± 0.00068		LANL-40	4.474 ± 0.046		0.0476 ± 0.0010		0.02154 ± 0.00067	
LANL - 3	6.142 ± 0.081		0.0674 ± 0.0021		0.02997 ± 0.00131		LANL-6	3.086 ± 0.025		0.0336 ± 0.0008		0.01557 ± 0.00056		LANL-41	5.132 ± 0.039		0.0546 ± 0.0011		0.02393 ± 0.00069	
LANL - 4	7.172 ± 0.091		0.0767 ± 0.0025		0.03441 ± 0.00141		LANL-7	1.576 ± 0.019		0.0174 ± 0.0006		0.00795 ± 0.00041		LANL-42	5.225 ± 0.040		0.0566 ± 0.0013		0.02497 ± 0.00076	
LANL - 5	7.264 ± 0.093		0.0785 ± 0.0023		0.03566 ± 0.00151		LANL-8	2.595 ± 0.085		0.0282 ± 0.0012		0.01309 ± 0.00046		LANL-43	4.962 ± 0.036		0.0532 ± 0.0010		0.02350 ± 0.00063	
LANL - 6	8.637 ± 0.120		0.0940 ± 0.0029		0.04198 ± 0.00172		LANL-9	2.953 ± 0.035		0.0318 ± 0.0008		0.01502 ± 0.00053		LANL-44	5.972 ± 0.061		0.0647 ± 0.0016		0.02883 ± 0.00111	
LANL - 7	7.121 ± 0.098		0.0760 ± 0.0023		0.03554 ± 0.00151		LANL-10	0.607 ± 0.011		0.0071 ± 0.0003		0.00311 ± 0.00026		LANL-45	5.420 ± 0.054		0.0586 ± 0.0015		0.02608 ± 0.00112	
LANL - 8	6.284 ± 0.090		0.0664 ± 0.0028		0.03003 ± 0.00141		LANL-11	0.838 ± 0.031		0.0095 ± 0.0005		0.00439 ± 0.00027		LLNL-1	7.408 ± 0.236					
LANL - 9	7.052 ± 0.244		0.0792 ± 0.0063		0.03261 ± 0.00321		LANL-12	2.341 ± 0.043		0.0256 ± 0.0008		0.01187 ± 0.00056		LLNL-2	3.763 ± 0.154					
LANL - 10	7.248 ± 0.097		0.0776 ± 0.0029		0.03512 ± 0.00161		LANL-13	5.716 ± 0.055		0.0625 ± 0.0012		0.02798 ± 0.00080		LLNL-3	2.853 ± 0.100					
LANL - 11	7.451 ± 0.099		0.0799 ± 0.0027		0.03585 ± 0.00151		LANL-14	2.631 ± 0.029		0.0289 ± 0.0009		0.01300 ± 0.00070		LLNL-4	2.827 ± 0.121					
LANL - 12	6.085 ± 0.106		0.0649 ± 0.0027		0.02910 ± 0.00151		LANL-15	4.599 ± 0.043		0.0488 ± 0.0011		0.02227 ± 0.00070		LLNL-5	4.130 ± 0.177					
LLNL - 1	6.576 ± 0.129						LANL - 16	5.006 ± 0.049		0.0544 ± 0.0013		0.02456 ± 0.00074		LLNL-6	1.475 ± 0.090					
LLNL - 2	7.215 ± 0.151						LANL - 17	4.295 ± 0.042		0.0468 ± 0.0012		0.02106 ± 0.00077		LLNL-7	0.113 ± 0.005					
LLNL - 3	7.185 ± 0.166						LANL - 18	0.044 ± 0.003		0.0005 ± 0.0001		0.00021 ± 0.00009		LLNL-8	4.713 ± 0.138					
LLNL - 4	7.967 ± 0.119						LANL - 19	2.767 ± 0.026		0.0297 ± 0.0007		0.01326 ± 0.00043		LLNL-9	3.744 ± 0.153					
LLNL - 5	7.421 ± 0.134						LANL - 20	0.076 ± 0.002		0.0008 ± 0.0002		0.00038 ± 0.00010		LLNL-10	2.119 ± 0.060					
LLNL - 6	7.326 ± 0.110						LANL - 21	0.110 ± 0.002		0.0013 ± 0.0001		0.00056 ± 0.00009		LLNL-11	4.687 ± 0.182					
LLNL - 7	7.081 ± 0.095						LANL - 22	0.165 ± 0.004		0.0017 ± 0.0002		0.00080 ± 0.00013		LLNL-12	5.013 ± 0.140					
LLNL - 8	7.718 ± 0.107						LANL - 23	1.232 ± 0.011		0.0129 ± 0.0005		0.00624 ± 0.00035		LLNL-13	2.711 ± 0.129					
LLNL - 9	8.025 ± 0.104						LANL - 24	3.887 ± 0.039		0.0427 ± 0.0012		0.01932 ± 0.00076		LLNL-14	0.022 ± 0.002					
LLNL - 10	6.676 ± 0.083						LANL - 25	0.745 ± 0.010		0.0078 ± 0.0004		0.00361 ± 0.00027		LLNL-15	2.816 ± 0.104					
LLNL - 11	6.768 ± 0.098						LANL - 26	1.164 ± 0.019		0.0126 ± 0.0006		0.00547 ± 0.00038		LLNL-16	0.202 ± 0.006					
LLNL - 12	6.867 ± 0.091						LANL - 27	4.447 ± 0.037		0.0479 ± 0.0011		0.02115 ± 0.00082		LLNL-17	1.010 ± 0.045					
LLNL - 13	6.354 ± 0.049						LANL - 28	3.008 ± 0.024		0.0328 ± 0.0008		0.01457 ± 0.00066		LLNL-18	0.234 ± 0.022					
LLNL - 14	7.070 ± 0.127						LANL - 29	3.344 ± 0.027		0.0360 ± 0.0009		0.01650 ± 0.00057		LLNL-19	0.315 ± 0.031					
LLNL - 15	6.772 ± 0.152						LANL - 30	0.192 ± 0.003		0.0020 ± 0.0002		0.00098 ± 0.00013		LLNL-20	0.350 ± 0.029					
LLNL - 16	6.575 ± 0.119						LANL - 31	0.301 ± 0.005		0.0033 ± 0.0003		0.00158 ± 0.00016								
LLNL - 17	7.059 ± 0.146						LANL - 32	0.052 ± 0.002		0.0005 ± 0.0001		0.00022 ± 0.00008								
LLNL - 18	11.843 ± 0.219						LANL - 33	0.034 ± 0.002		0.0003 ± 0.0001		0.00017 ± 0.00005								
LLNL - 19	8.162 ± 0.133						LANL - 34	0.126 ± 0.002		0.0013 ± 0.0001		0.00061 ± 0.00007								
							LANL - 35	0.288 ± 0.004		0.0029 ± 0.0002		0.00146 ± 0.00014								

01 Table 6 (cont.)

U3	$^{235}\text{U}/^{238}\text{U}$	2σ	$^{234}\text{U}/^{238}\text{U}$	2σ	$^{236}\text{U}/^{238}\text{U}$	2σ	U3 (cont.)	$^{235}\text{U}/^{238}\text{U}$	2σ	$^{234}\text{U}/^{238}\text{U}$	2σ	$^{236}\text{U}/^{238}\text{U}$	2σ
LANL - 1	3.236 ± 0.076		0.0343 ± 0.0023		0.01582 ± 0.00149		LLNL - 16	0.413 ± 0.026					
LANL - 2	2.180 ± 0.034		0.0242 ± 0.0012		0.01097 ± 0.00082		LLNL - 17	1.154 ± 0.033					
LANL - 3	3.118 ± 0.039		0.0337 ± 0.0012		0.01443 ± 0.00081		LLNL - 18	0.241 ± 0.010					
LANL - 4	3.768 ± 0.047		0.0403 ± 0.0013		0.01766 ± 0.00093		LLNL - 19	0.899 ± 0.056					
LANL - 5	3.838 ± 0.043		0.0423 ± 0.0014		0.01807 ± 0.00098		LLNL - 20	2.627 ± 0.079					
LANL - 6	3.898 ± 0.048		0.0425 ± 0.0015		0.01957 ± 0.00086		LLNL - 21	3.042 ± 0.078					
LANL - 7	3.662 ± 0.029		0.0401 ± 0.0009		0.01783 ± 0.00062		LLNL - 22	4.324 ± 0.143					
LANL - 8	1.133 ± 0.012		0.0127 ± 0.0006		0.00546 ± 0.00038								
LANL - 9	2.047 ± 0.020		0.0221 ± 0.0007		0.01003 ± 0.00046		U4	$^{235}\text{U}/^{238}\text{U}$	2σ	$^{234}\text{U}/^{238}\text{U}$	2σ	$^{236}\text{U}/^{238}\text{U}$	2σ
LANL - 10	2.923 ± 0.026		0.0316 ± 0.0008		0.01412 ± 0.00053		LANL - 1	4.708 ± 0.070		0.0491 ± 0.0028		0.02298 ± 0.00159	
LANL - 11	4.030 ± 0.040		0.0430 ± 0.0010		0.01971 ± 0.00070		LANL - 2	4.596 ± 0.066		0.0523 ± 0.0024		0.02369 ± 0.00164	
LANL - 12	3.779 ± 0.038		0.0399 ± 0.0012		0.01795 ± 0.00076		LANL - 3	4.635 ± 0.063		0.0496 ± 0.0026		0.02346 ± 0.00161	
LANL - 13	4.585 ± 0.045		0.0495 ± 0.0013		0.02307 ± 0.00086		LANL - 4	3.935 ± 0.067		0.0430 ± 0.0024		0.02165 ± 0.00161	
LANL - 14	5.712 ± 0.073		0.0613 ± 0.0021		0.02850 ± 0.00123		LANL - 5	3.811 ± 0.061		0.0416 ± 0.0022		0.01800 ± 0.00136	
LANL - 15	4.713 ± 0.064		0.0501 ± 0.0016		0.02293 ± 0.00103		LANL - 6	3.075 ± 0.038		0.0332 ± 0.0017		0.01539 ± 0.00121	
LANL - 16	3.834 ± 0.042		0.0413 ± 0.0016		0.01855 ± 0.00084		LANL - 7	3.218 ± 0.034		0.0344 ± 0.0018		0.01570 ± 0.00116	
LANL - 17	2.517 ± 0.029		0.0271 ± 0.0009		0.01267 ± 0.00063		LANL - 8	3.953 ± 0.049		0.0443 ± 0.0022		0.01979 ± 0.00150	
LANL - 18	3.208 ± 0.033		0.0344 ± 0.0011		0.01534 ± 0.00071		LANL - 9	4.204 ± 0.052		0.0461 ± 0.0022		0.02045 ± 0.00146	
LANL - 19	4.629 ± 0.046		0.0506 ± 0.0015		0.02311 ± 0.00087		LANL - 10	3.869 ± 0.047		0.0423 ± 0.0024		0.01970 ± 0.00149	
LANL - 20	4.520 ± 0.052		0.0483 ± 0.0014		0.02231 ± 0.00088		LANL - 11	5.225 ± 0.066		0.0565 ± 0.0026		0.02547 ± 0.00175	
LANL - 21	1.103 ± 0.019		0.0118 ± 0.0006		0.00536 ± 0.00041		LANL - 12	4.737 ± 0.068		0.0491 ± 0.0024		0.02342 ± 0.00165	
LANL - 22	0.522 ± 0.008		0.0055 ± 0.0004		0.00248 ± 0.00027		LANL - 13	5.237 ± 0.064		0.0588 ± 0.0028		0.02433 ± 0.00177	
LANL - 23	4.121 ± 0.042		0.0442 ± 0.0013		0.02018 ± 0.00093		LANL - 14	5.150 ± 0.066		0.0565 ± 0.0030		0.02551 ± 0.00185	
LANL - 24	4.034 ± 0.039		0.0434 ± 0.0013		0.01959 ± 0.00075		LANL - 15	5.164 ± 0.070		0.0557 ± 0.0033		0.02430 ± 0.00196	
LANL - 25	5.317 ± 0.054		0.0576 ± 0.0015		0.02605 ± 0.00088		LANL - 16	5.344 ± 0.069		0.0593 ± 0.0032		0.02682 ± 0.00198	
LANL - 26	6.565 ± 0.058		0.0708 ± 0.0014		0.03211 ± 0.00099		LLNL - 1	5.890 ± 0.135					
LANL - 27	4.414 ± 0.053		0.0477 ± 0.0013		0.02176 ± 0.00088		LLNL - 2	6.246 ± 0.115					
LANL - 28	5.152 ± 0.053		0.0572 ± 0.0014		0.02466 ± 0.00086		LLNL - 3	5.707 ± 0.111					
LLNL - 1	5.454 ± 0.115						LLNL - 4	6.092 ± 0.114					
LLNL - 2	4.394 ± 0.125						LLNL - 5	1.904 ± 0.053					
LLNL - 3	5.478 ± 0.114						LLNL - 6	3.924 ± 0.076					
LLNL - 4	4.282 ± 0.101						LLNL - 7	2.956 ± 0.055					
LLNL - 5	3.971 ± 0.106						LLNL - 8	2.938 ± 0.061					
LLNL - 6	1.911 ± 0.079						LLNL - 9	4.317 ± 0.115					
LLNL - 7	3.158 ± 0.088						LLNL - 10	5.102 ± 0.124					
LLNL - 8	4.092 ± 0.096						LLNL - 11	5.435 ± 0.123					
LLNL - 9	4.326 ± 0.100						LLNL - 12	5.859 ± 0.130					
LLNL - 10	6.779 ± 0.178						LLNL - 13	5.162 ± 0.144					
LLNL - 11	4.901 ± 0.108						LLNL - 14	4.669 ± 0.101					
LLNL - 12	4.469 ± 0.110						LLNL - 15	3.047 ± 0.080					
LLNL - 13	6.114 ± 0.191						LLNL - 16	5.847 ± 0.148					
LLNL - 14	4.476 ± 0.119						LLNL - 17	2.462 ± 0.070					
LLNL - 15	3.076 ± 0.058						LLNL - 18	3.314 ± 0.075					
							LLNL - 19	2.113 ± 0.049					

602 Table A1

Standard	$^{235}\text{U}/^{238}\text{U}$		$^{234}\text{U}/^{238}\text{U}$		$^{236}\text{U}/^{238}\text{U}$	
		2σ		2σ		2σ
CRM U500 Certificate	0.9997	± 0.0014	0.010422	± 0.000019	0.001519	± 0.000006
LLNL (350 $\mu\text{g/g}$ U)	0.9618	± 0.0013	0.010044	± 0.000006	0.001479	± 0.000006
Deviation (%)	-3.79	± 0.19	-3.63	± 0.19	-2.62	± 0.57
LANL (3,500 $\mu\text{g/g}$ U)	0.9949	± 0.0014	0.010371	± 0.000006	0.001521	± 0.000005
Deviation (%)	-0.48	± 0.20	-0.49	± 0.19	0.15	± 0.53

603 Table A2

Analysis #	$^{235}\text{U}/^{238}\text{U}$	2σ
1	0.974 ±	0.014
2	0.955 ±	0.011
3	0.965 ±	0.008
4	0.961 ±	0.010
5	0.967 ±	0.008
6	0.955 ±	0.009
7	0.968 ±	0.011
8	0.960 ±	0.014
9	0.975 ±	0.009
10	0.970 ±	0.012
11	0.968 ±	0.010
12	0.970 ±	0.012
13	0.968 ±	0.007
14	0.969 ±	0.014
15	0.971 ±	0.017
16	0.959 ±	0.014
17	0.974 ±	0.014
18	0.965 ±	0.019
19	0.957 ±	0.011
20	0.956 ±	0.023
21	0.979 ±	0.012
22	0.969 ±	0.007
23	0.955 ±	0.010

Analysis #	Mode	$^{235}\text{U}/^{238}\text{U}$	2σ	$^{234}\text{U}/^{238}\text{U}$	2σ	$^{236}\text{U}/^{238}\text{U}$	2σ
1	mono	1.0042	± 0.0018	0.01059	± 0.00005	0.00152	± 0.00002
2	mono	1.0057	± 0.0018	0.01051	± 0.00006	0.00153	± 0.00002
3	mono	1.0074	± 0.0041	0.01052	± 0.00007	0.00154	± 0.00002
4	mono	1.0084	± 0.0055	0.01057	± 0.00008	0.00154	± 0.00002
5	mono	1.0018	± 0.0043	0.01050	± 0.00008	0.00153	± 0.00003
6	mono	1.0066	± 0.0059	0.01054	± 0.00010	0.00155	± 0.00002
7	mono	1.0040	± 0.0010	0.01053	± 0.00005	0.00154	± 0.00002
8	multi	1.0022	± 0.0016	0.01044	± 0.00011	0.00154	± 0.00004
9	multi	1.0011	± 0.0016	0.01047	± 0.00012	0.00152	± 0.00005
10	multi	1.0024	± 0.0021	0.01037	± 0.00014	0.00154	± 0.00004
11	multi	1.0004	± 0.0019	0.01047	± 0.00012	0.00151	± 0.00005
12	multi	1.0011	± 0.0017	0.01039	± 0.00014	0.00152	± 0.00005
13	multi	1.0013	± 0.0017	0.01032	± 0.00012	0.00155	± 0.00005
14	multi	1.0020	± 0.0018	0.01044	± 0.00012	0.00151	± 0.00005
15	multi	1.0011	± 0.0021	0.01032	± 0.00012	0.00156	± 0.00005
16	multi	1.0009	± 0.0017	0.01039	± 0.00012	0.00148	± 0.00006
17	multi	1.0027	± 0.0023	0.01046	± 0.00013	0.00149	± 0.00005

605 Table B1

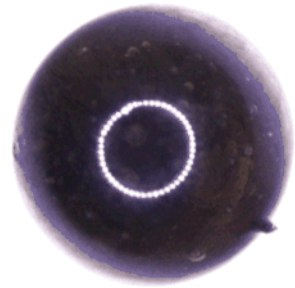
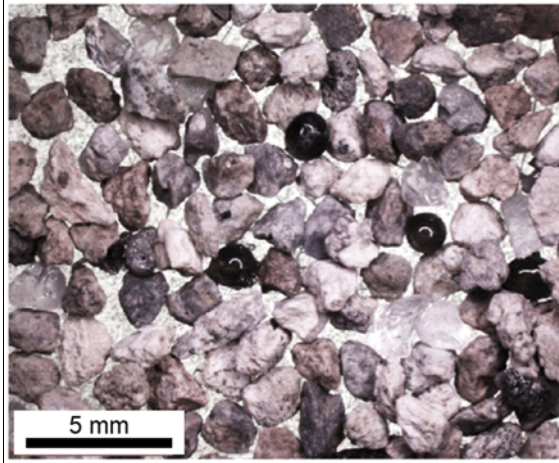
Sample U3					Sample U4						
$^{235}\text{U}/^{238}\text{U}$	2σ	$\mu\text{g/g}$	2σ		$^{235}\text{U}/^{238}\text{U}$	2σ	$\mu\text{g/g}$	2σ			
4.394	±	0.125	12.0	±	1.1	5.890	±	0.135	19.4	±	2.7
5.478	±	0.114	13.1	±	1.2	6.246	±	0.115	17.9	±	2.4
4.282	±	0.101	13.4	±	1.3	5.707	±	0.111	17.6	±	2.4
3.971	±	0.106	11.6	±	1.0	6.092	±	0.114	16.1	±	2.2
1.911	±	0.079	4.4	±	0.4	1.904	±	0.053	8.3	±	1.1
3.158	±	0.088	12.2	±	1.0	3.924	±	0.076	11.9	±	1.6
4.092	±	0.096	11.8	±	1.1	2.956	±	0.055	11.1	±	1.5
4.326	±	0.100	11.4	±	1.0	2.938	±	0.061	10.7	±	1.5
6.779	±	0.178	18.7	±	1.7	4.317	±	0.115	12.4	±	1.7
4.901	±	0.108	10.4	±	0.9	5.102	±	0.124	15.8	±	2.1
4.469	±	0.110	10.6	±	0.9	5.435	±	0.123	12.4	±	1.7
6.114	±	0.191	8.5	±	1.1	5.859	±	0.130	13.8	±	1.9
4.476	±	0.119	10.6	±	0.9	5.162	±	0.144	13.4	±	1.9
3.076	±	0.058	11.2	±	1.0	4.669	±	0.101	13.1	±	1.8
0.413	±	0.026	3.5	±	0.3	3.047	±	0.080	11.2	±	1.5
1.154	±	0.033	4.8	±	0.4	5.847	±	0.148	14.5	±	2.0
0.241	±	0.010	4.1	±	0.3	2.462	±	0.070	9.0	±	1.2
0.899	±	0.056	5.6	±	0.5	3.314	±	0.075	7.1	±	1.1
2.627	±	0.079	9.5	±	0.9	2.113	±	0.049	4.7	±	0.6
3.042	±	0.078	15.7	±	1.5						
4.324	±	0.143	13.5	±	1.2						

606

607

608

Fig 1



609

610

611

Fig 2.

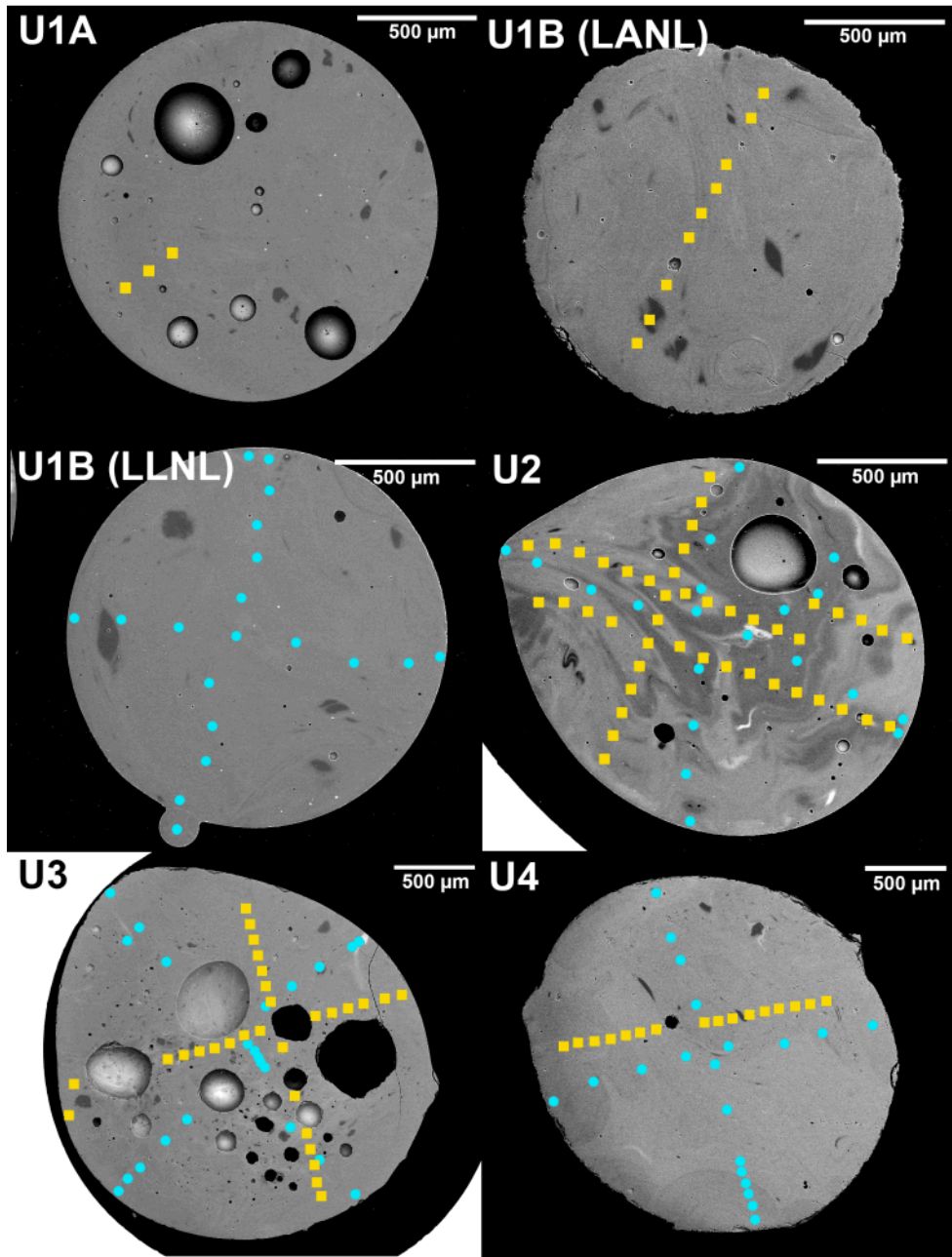
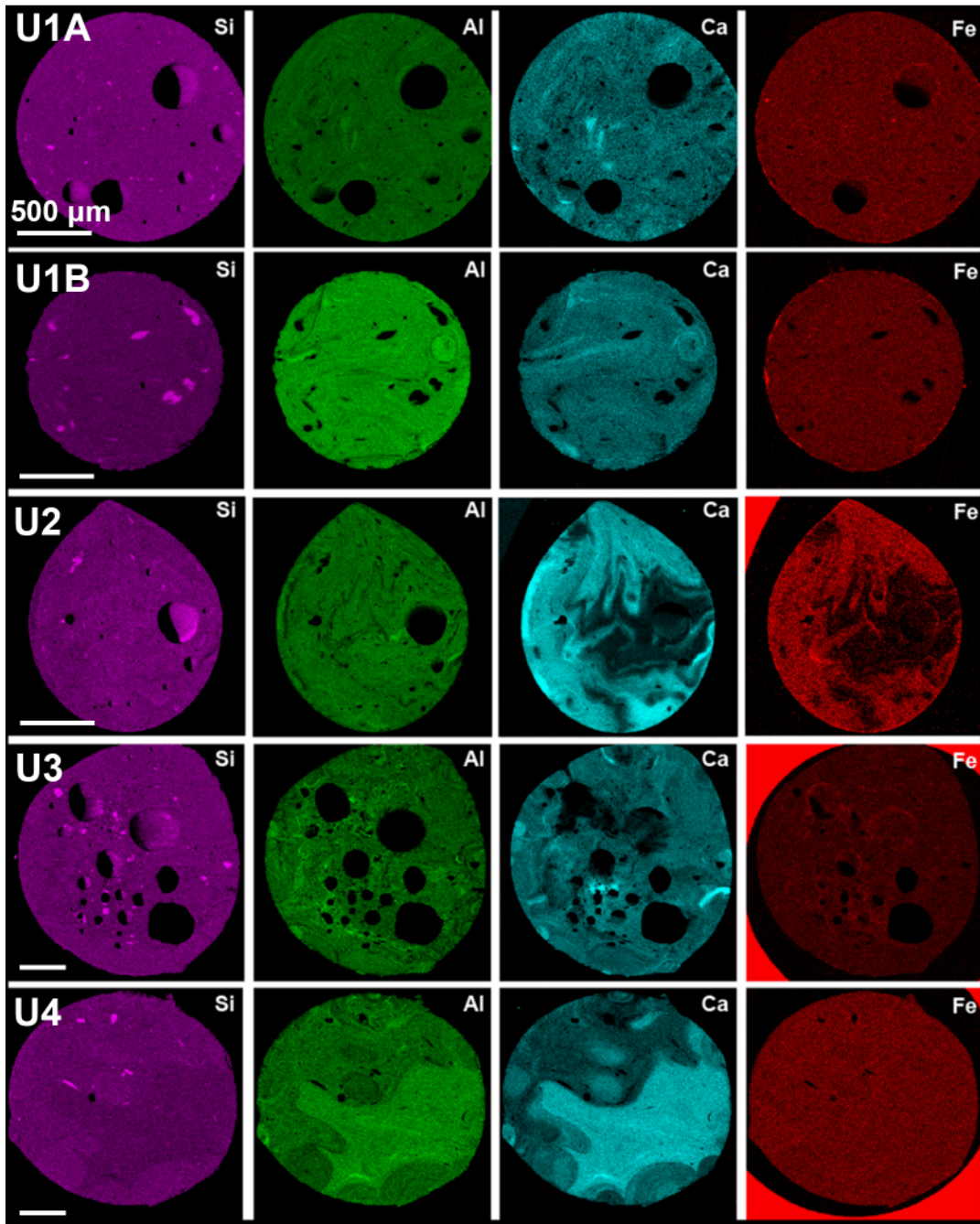
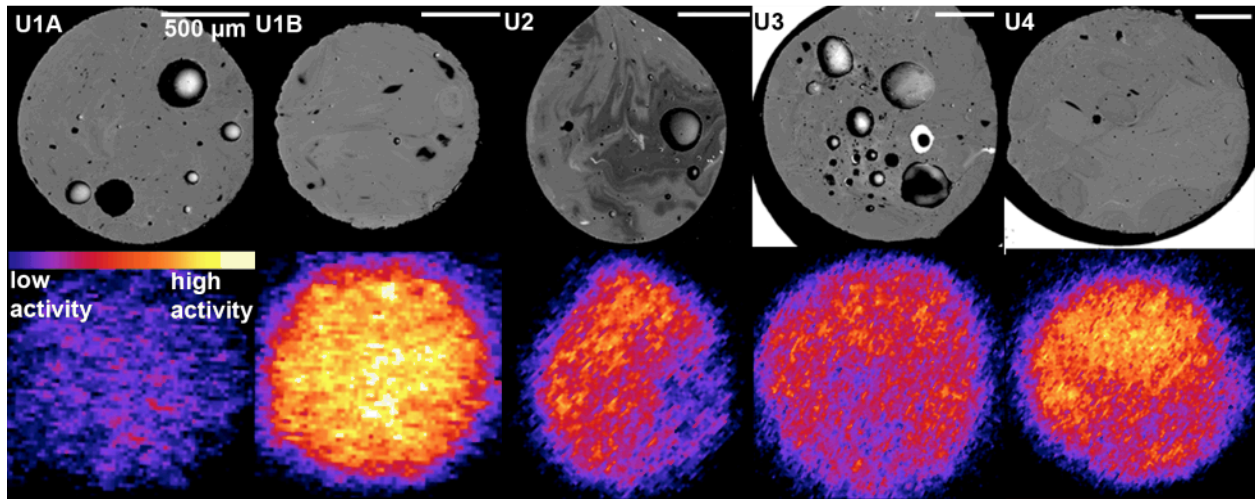


Fig. 3



618

Fig. 4

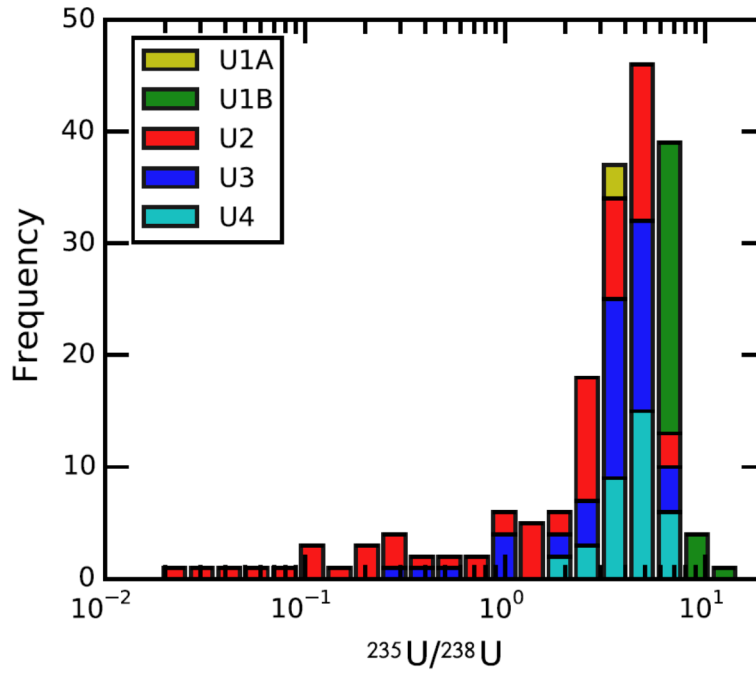


619

620

622

Fig. 5

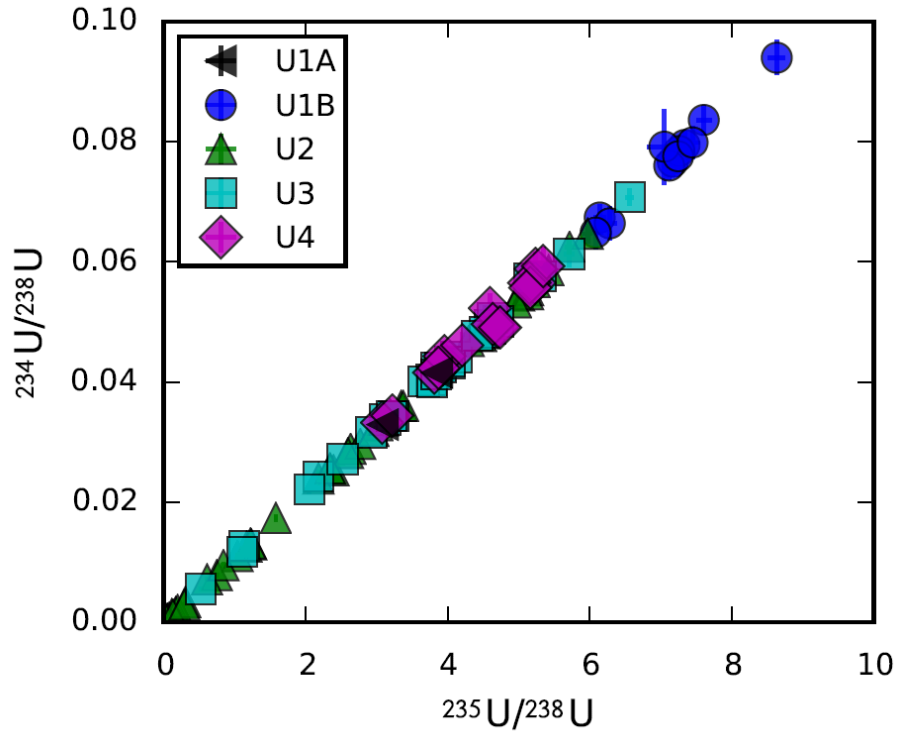


623

624

625

Fig. 6

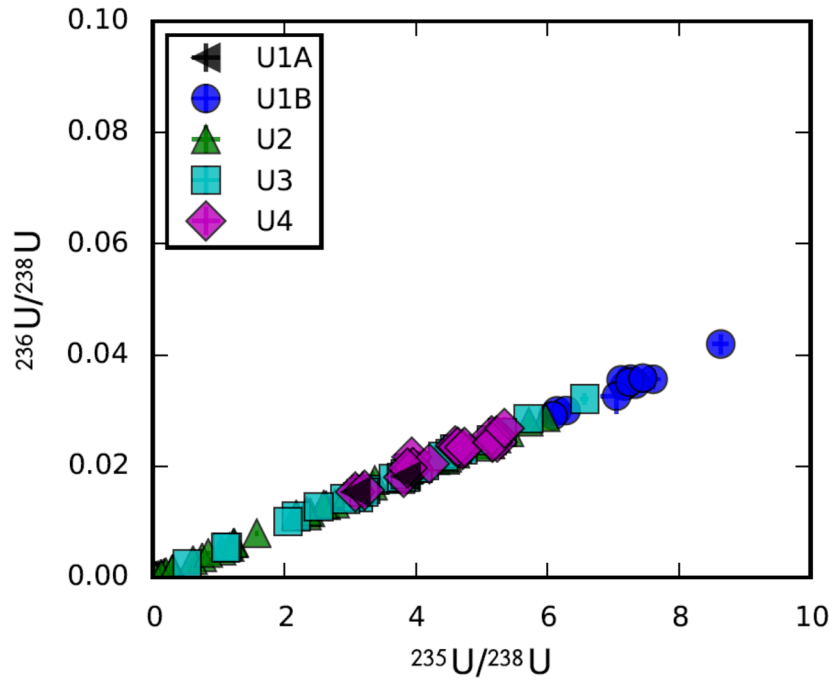


626

627

628

Fig. 7

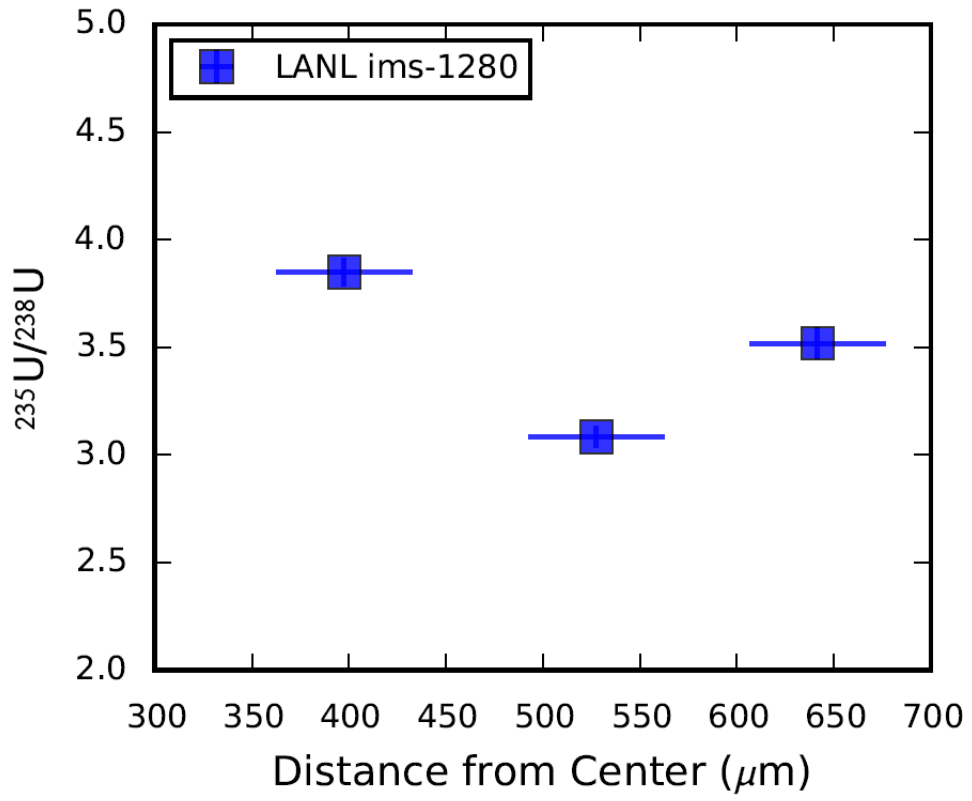


629

630

631

Fig. 8

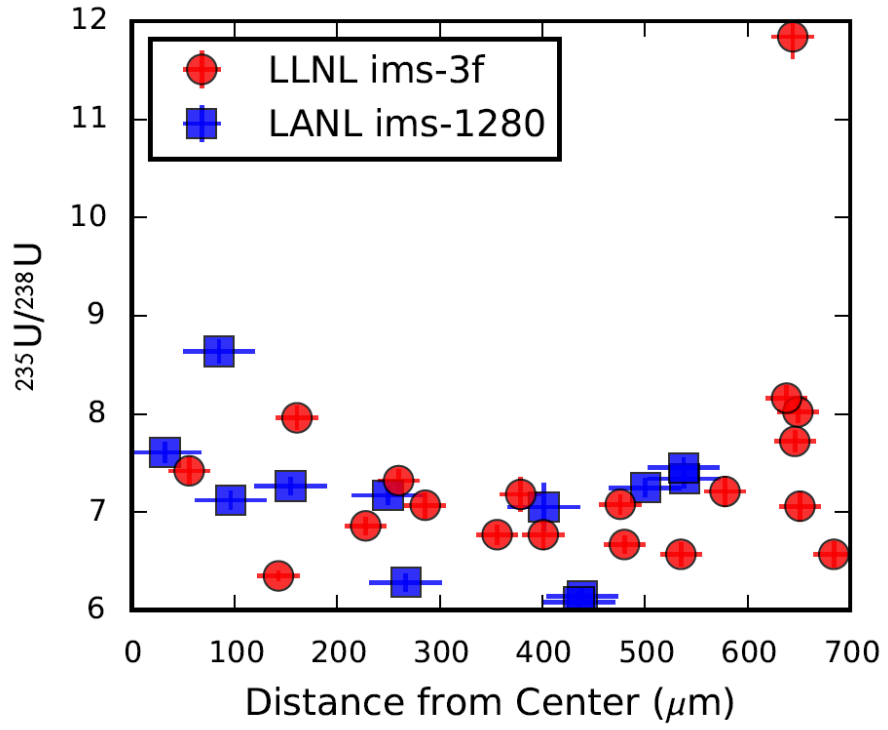


632

633

634

Fig. 9

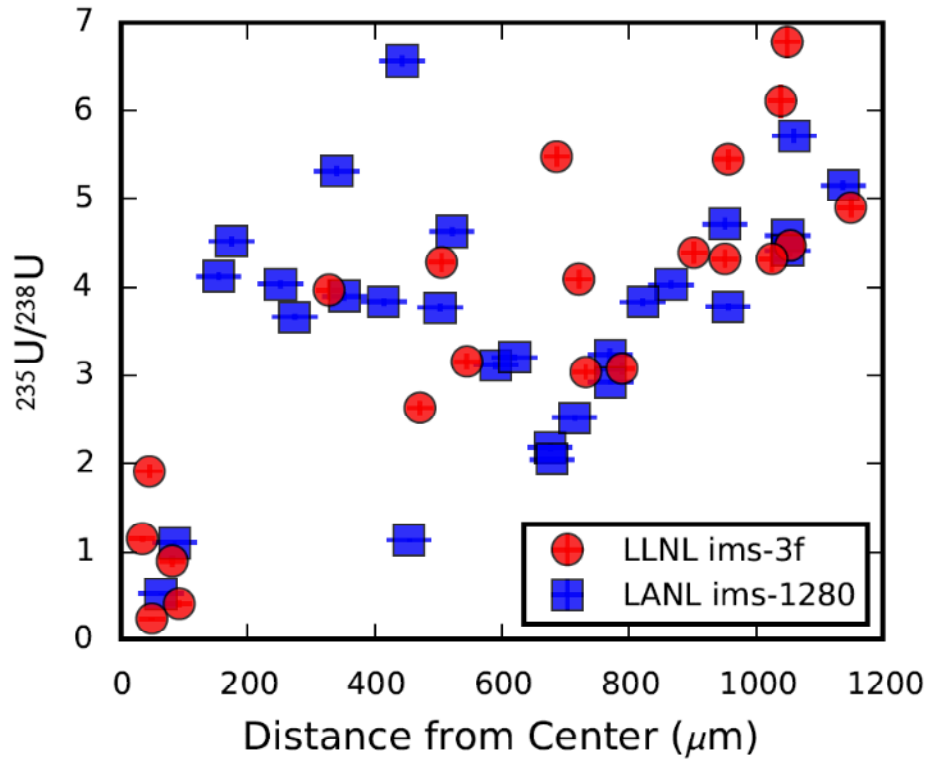


635

636

637

Fig. 10

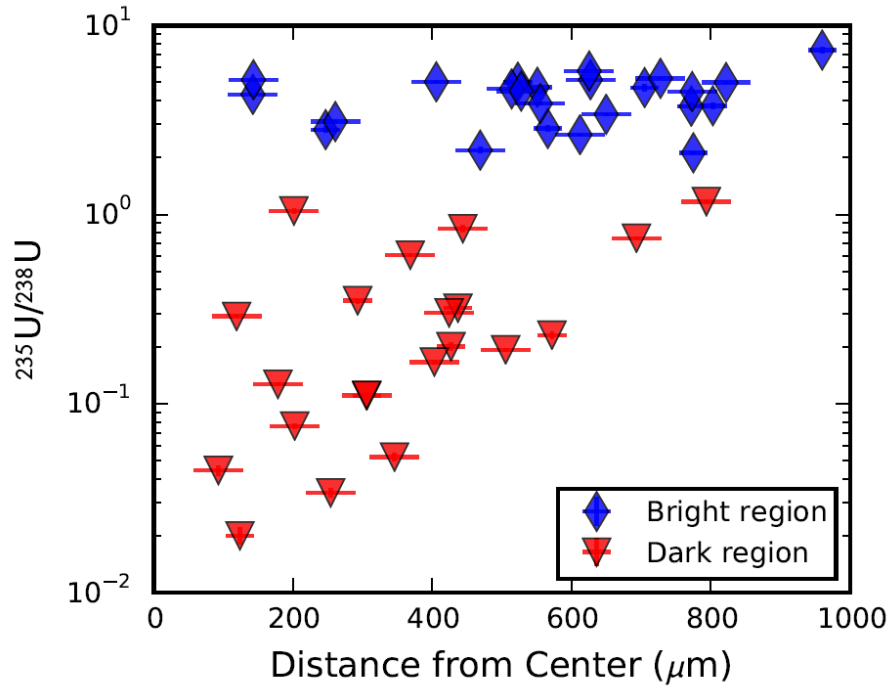


638

639

640

Fig. 11

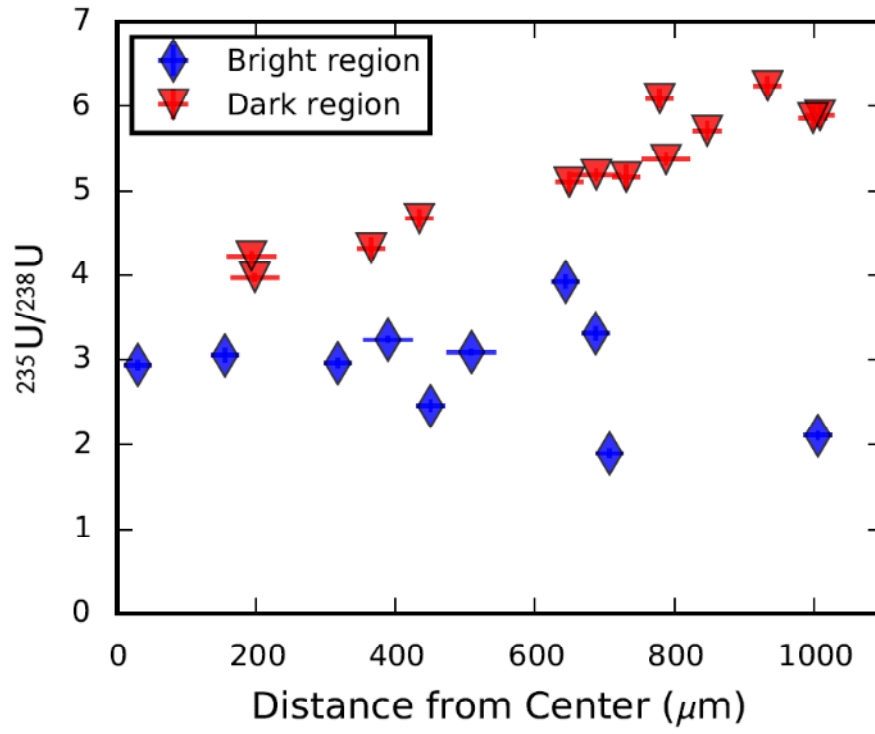


641

642

643

Fig. 12

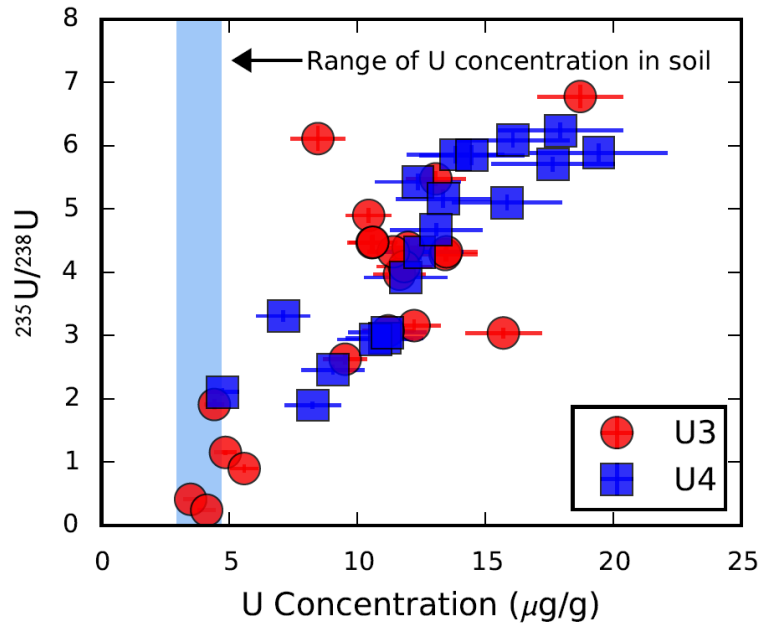


644

645

646

Fig. 13

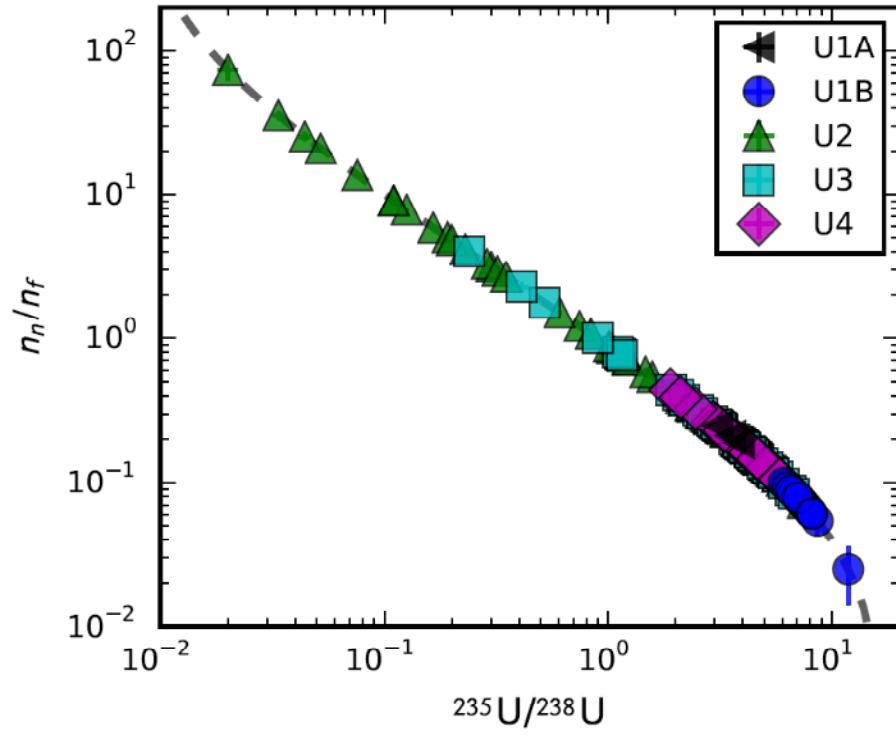


647

648

649

Fig. 14



650